ADAPTIVE, SECOND-ORDER, UNCONDITIONALLY STABLE PARTITIONED METHOD FOR FLUID-STRUCTURE INTERACTION

MARTINA BUKAČ * AND CATALIN TRENCHEA †

Abstract. We propose a novel, time adaptive, strongly-coupled partitioned method for the interaction between a viscous, incompressible fluid and a thin elastic structure. The time integration is based on the refactorized Cauchy's one–legged '$\theta-$like' method, which consists of a backward Euler method using a $\theta\tau_n$–time step and a forward Euler method using a $(1-\theta)\tau_n$–time step. The bulk of the computation is done by the backward Euler method, as the forward Euler step is equivalent to (and implemented as) a linear extrapolation. The variable τ_n–time step integration scheme is combined with the partitioned, kinematically coupled $\beta-$scheme, used to decouple the fluid and structure sub–problems. In the backward Euler step, the two sub–problems are solved in a partitioned sequential manner, and iterated until convergence. Then, the fluid and structure sub–problems are post–processed /extrapolated in the forward Euler step, and finally the τ_n–time step is adapted. The refactorized Cauchy's one–legged '$\theta-$like' method used in the development of the proposed method is equivalent to the midpoint rule when $\theta = \frac{1}{2}$, in which case the method is non–dissipative and second–order accurate. We prove that the sub–iterative process of our algorithm is linearly convergent, and that the method is unconditionally stable when $\theta \geq \frac{1}{2}$. The numerical examples explore the properties of the method when both fixed and variable time steps are used, and in both cases shown an excellent agreement with the reference solution.

Key words. time adaptivity; fluid-structure interaction; partitioned method; second-order accuracy; unconditional stability

1. Introduction. In realistic flow problems described by partial differential equations (PDEs), where the dynamics are not known, or in which the variables are changing rapidly, the robust, adaptive time-stepping is central to accurately and efficiently predict the long–term behavior of the solution. This is especially important in the coupled flow problems, such as the fluid–structure interaction (FSI), which often exhibit complex dynamic behavior. While the adaptive spatial mesh refinement techniques are well established and widely used, the adaptive time–stepping methods for PDEs are less mature, needing delicate synchronization steps which involve interpolation, extrapolation or projection. These operations can have adverse effects on the stability, and can destroy important geometric properties of the scheme (e.g. the conservation of invariants). Even in the case of the ordinary differential equations, most linear multistep methods [24, 33], when considered with variable time steps, do not preserve the zero–stability or A–stability properties of the constant time step versions. For example, the trapezoidal (Crank-Nicolson) method in the constant step case is A–stable but not B–stable [1]. However, the variable step version of the trapezoidal method is unstable [24, 41, 42, 45]. Similarly, the second–order backward differentiation formula loses zero–stability and A–stability when used with a variable step size.

Recently, the midpoint rule was considered in an alternative, backward Euler (BE)–forward Euler (FE) formulation, and was proved to be B–stable when applied with a variable time step [17]. The same was shown for a $\theta-$like generalization of the midpoint rule, referred to as the refactorized Cauchy's one-legged '$\theta-$like' method [17]. In this work, this method is applied together with a partitioning approach to approximate the solution of the interaction between an incompressible, viscous fluid and a thin elastic structure. To best of our knowledge, this is the first unconditionally stable, second-order accurate, adaptive, partitioned method for FSI problems.

Adaptive time–stepping methods for FSI problems have received limited attention in the literature, especially from the analytical perspective. A novel, adaptive time–stepping method for a monolithic FSI problem based on the a posteriori error estimation was proposed in [40]. The error of the fully implicit scheme is estimated with the help of an auxiliary explicit scheme. The proposed method is tested on several numerical examples. The authors in [26] considered a nonlinear FSI problem based on the arbitrary Lagrangian–Eulerian approach and solved the equations using an adaptive Fractional–Step–theta scheme method applied to the monolithic system. They based the time adaptivity process on a rigorous derivation of dual–weighted sensitivity measures and heuristic truncation–based time step control. In order to apply the dual–weighted residual method, a Galerkin interpretation of the Fractional–Step–theta scheme was

*Department of Applied and Computational Mathematics and Statistics, University of Notre Dame, Notre Dame, IN 46556, USA.

†Department of Mathematics, University of Pittsburgh, Pittsburgh, PA 15260, USA.

considered. The proposed methodology was tested on several numerical examples. In [25], the interaction between a viscous fluid and a rigid body under turbulent flow was studied. The authors combined the large eddy simulation based on implicit turbulence modeling with time–space adaptive techniques in arbitrary Lagrangian–Eulerian framework. We also mention the work in [8, 9] where a time–adaptive fluid–structure interaction method for thermal coupling is used to model the cooling processes in heat treatment of steel. In particular, the authors consider the surface coupling of the compressible Navier–Stokes equations bordering at one part of the surface with the heat equation in a solid region. The fluid and the heat equation are solved in parallel in a partitioned manner. The resulting method was empirically shown to be second–order accurate, which was used to implement a simple time step control.

While the methods listed above have been extensively numerically verified, they have not been analyzed numerically. Furthermore, in case of the interaction between an incompressible, viscous fluid and an elastic structure, only monolithic adaptive methods have been considered, while many different partitioned methods have been proposed when the time step is fixed [3–5, 7, 12, 14, 15, 27, 39, 43, 44, 46].

In this work, we propose a novel, adaptive, partitioned algorithm for the interaction between an incompressible, viscous fluid and a thin, elastic structure. The time discretization in the proposed method is based on the refactorized Cauchy's one–legged '$\theta-$like' scheme [17], which is equivalent to the midpoint rule (and, therefore, second–order accurate) when $\theta = \frac{1}{2}$. This method is adapted and combined with the partitioned, kinematically coupled $\beta-$scheme, proposed in [12, 13]. However, unlike the kinematically coupled $\beta-$scheme, the proposed adaptive method is strongly coupled. In particular, the fluid and structure sub–problems, based on the BE discretization and the kinematically coupled $\beta-$scheme, are solved sequentially and iterated until convergence. Then, the converged solutions of the two sub–problems are post-processed using an extrapolation (equivalent to the FE scheme), and the time step is adapted. To adapt the time step, we use a local truncation error estimator based on the solution obtained using the Adams–Bashforth two-step (AB2) method. To discretize the problem in space, we use the finite element method. As commonly done in the literature in order to simplify numerical analysis, we assume that the fluid is modeled using the Stokes equations, that the structure displacement is infinitesimal and that the FSI problem is linear [6, 13, 18, 27]. Using these assumptions, we prove that the sub–iterative process converges *linearly*, and that the proposed method is unconditionally energy bounded, hence stable, when $\theta \geq \frac{1}{2}$.

We note that the proposed method is novel even when considered with a fixed time step, in which case it can be seen as a second–order extension (when $\theta = \frac{1}{2}$) of the kinematically coupled $\beta-$scheme. Hence, in the numerical examples we investigate the convergence rates of the proposed method when a fixed time step is used, as well as the accuracy properties of both fixed and variable time–stepping versions. The results are compared with the kinematically coupled $\beta-$scheme, which has been shown to be first–order accurate when $\beta = 1$. Our computational study indicates an excellent agreement between the reference solution and the results obtained using the proposed method with both fixed and variable time steps, and provide an insight in the selection of parameters used in the adaptive process to exploit the benefits of time adaptivity.

The rest of this paper is organized as follows. The FSI problem is outlined in Section 2. The numerical method, together with the convergence and stability analysis, is presented in Section 3. The computation of the local truncation error is shown in Section 4, and the numerical examples are presented in Section 5. Finally, the conclusions are drawn in Section 6.

2. Description of the problem. Let $\Omega \subset \mathbb{R}^d$, $d = 2, 3$ be an open, smooth set, occupied by an incompressible, viscous, Newtonian fluid, such that $\partial\bar{\Omega} = \Gamma \cup \Gamma_{in} \cup \Gamma_{out}$, where Γ represents the elastic structure, Γ_{in} represents the inlet and Γ_{out} represents the outlet (see Figure 2.1). We assume that the flow is laminar, that the structure undergoes infinitesimal displacements and that the fluid-structure interaction is linear. These are common assumptions in the analysis of partitioned schemes for FSI problems [6, 13, 18, 27].

We model the fluid using the time–dependent Stokes equations in a fixed domain Ω, given as

$$\rho_f \partial_t \boldsymbol{u} = \nabla \cdot \boldsymbol{\sigma}(\boldsymbol{u}, p) + \boldsymbol{f}_f \qquad \text{in } \Omega \times (0, T), \tag{2.1a}$$

$$\nabla \cdot \boldsymbol{u} = 0 \qquad \text{in } \Omega \times (0, T), \tag{2.1b}$$

$$\boldsymbol{\sigma}(\boldsymbol{u}, p)\boldsymbol{n} = -p_{in}(t)\boldsymbol{n} \qquad \text{on } \Gamma_{in} \times (0, T), \tag{2.1c}$$

$$\boldsymbol{\sigma}(\boldsymbol{u}, p)\boldsymbol{n} = -p_{out}(t)\boldsymbol{n} \qquad \text{on } \Gamma_{out} \times (0, T), \tag{2.1d}$$

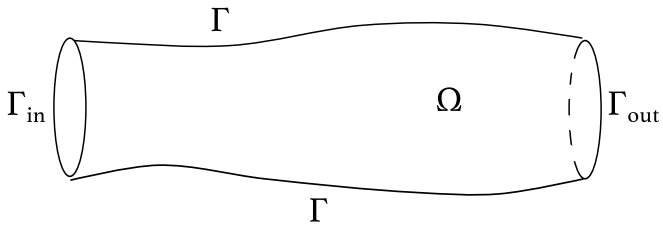

Fig. 2.1: Fluid domain Ω. The lateral boundary Γ represents an elastic structure.

$$\boldsymbol{u}(.,0) = \boldsymbol{u}^0 \qquad \text{in } \Omega, \tag{2.1e}$$

where $\boldsymbol{u} = (u_i)_{i=1,\dots,d}$ is the fluid velocity, p is the fluid pressure, ρ_f is the fluid density and $\boldsymbol{\sigma}(\boldsymbol{u}, p) = -p\boldsymbol{I} + 2\mu\boldsymbol{D}(\boldsymbol{u})$ is the fluid stress tensor, where $\boldsymbol{D}(\boldsymbol{u}) = (\nabla\boldsymbol{u} + (\nabla\boldsymbol{u})^T)/2$ is the strain rate tensor and μ is the fluid viscosity. The volume forcing term acting on the fluid is denoted by $\boldsymbol{f}_f$. At the inlet and outlet boundaries, Neumann boundary conditions (2.1c)-(2.1d) are prescribed, where $\boldsymbol{n}$ denotes the outward normal to the fluid domain boundary, and p_{in} and p_{out} are the prescribed inflow and outflow forces, respectively. Initially, the fluid is assumed to be at rest, as prescribed in (2.1e).

To describe the structure elastodynamics, we use a linearly elastic, lower-dimensional model, given by

$$\rho_s h\partial_{tt}\boldsymbol{\eta} + \mathcal{L}_s\boldsymbol{\eta} = \boldsymbol{f}_s \qquad \text{on } \Gamma \times (0,T), \tag{2.2a}$$
$$\boldsymbol{\eta} = \boldsymbol{0} \qquad \text{on } \partial\Gamma \times (0,T), \tag{2.2b}$$
$$\boldsymbol{\eta}(.,0) = \boldsymbol{\eta}^0,\ \partial_t\boldsymbol{\eta}(.,0) = \boldsymbol{\eta}_v^0 \qquad \text{on } \Gamma, \tag{2.2c}$$

where $\boldsymbol{\eta} = (\eta_i)_{i=1,\dots,d}$ denotes the displacement, ρ_s denotes the density, h denotes the structure thickness and $\boldsymbol{f}_s$ is a vector of surface density of the force applied to the structure. Operator $\mathcal{L}_s$ describes the structure's elastic behavior. Specific choices of $\mathcal{L}_s$ are detailed in Section 5. We assume that the structure is clamped at the edges (2.2b) and initially at rest, with zero displacement from the initial configuration (2.2c).

We define an inner-product and a norm associated with the structure operator, given by

$$a_s(\boldsymbol{\eta}, \boldsymbol{\zeta}) = \int_\Gamma \mathcal{L}_s\boldsymbol{\eta} \cdot \boldsymbol{\zeta} dS, \qquad \|\boldsymbol{\eta}\|_S^2 = a_s(\boldsymbol{\eta}, \boldsymbol{\eta}).$$

We assume that operator $\mathcal{L}_s : D(\mathcal{L}_s) \subset H^1(\Gamma) \to L^2(\Gamma)$ is a maximal monotone operator [11], such that a Poincaré type inequality holds

$$\|\boldsymbol{\eta}\|_{L^2(\Gamma)} \leq C_{P,S}\|\boldsymbol{\eta}\|_S,$$

and the norm $\|\cdot\|_S$ is equivalent to the $H^1(\Gamma)$ norm. One example of such operator is the one associated with the linearly elastic Koiter shell model used in [16].

To couple the fluid and the structure, we prescribe the kinematic and dynamic coupling conditions. The kinematic coupling condition (no–slip condition) enforces the continuity of velocities at the fluid–structure interface, given by

$$\boldsymbol{u} = \partial_t\boldsymbol{\eta} \quad \text{on } \Gamma \times (0,T). \tag{2.3}$$

The dynamic coupling condition enforces the conservation of momentum, given by

$$\boldsymbol{f}_s = -\boldsymbol{\sigma}(\boldsymbol{u}, p)\boldsymbol{n} \quad \text{on } \Gamma \times (0,T). \tag{2.4}$$

Equations (2.1a)-(2.4) define a linear fluid–structure interaction problem, which has a well–defined energy [13, 43].

3. Numerical scheme. The proposed method is based on the kinematically coupled β–scheme proposed in [12, 13], combined with the refactorized Cauchy's one–legged 'θ–like' method [17]. To present the main steps of the proposed method, we consider a general evolution equation given by

$$y'(t) = f(t, y(t)), \quad t \in (a, b].$$

To solve this problem numerically with an adaptive time step, we apply the Cauchy's one–legged 'θ–like' method [20], given as follows

$$\frac{y^{n+1} - y^n}{\tau^n} = f(t^{n+\theta_n}, y^{n+\theta_n}) \quad \text{for } \theta_n \in [0, 1], \tag{3.1}$$

where $\{t^n\}_{0 \le n \le N}$ are mesh points based on a variable time step τ^n such that $t^{n+1} = t^n + \tau^n$, and $t^{n+\theta_n} = t^n + \theta_n \tau^n$. Furthermore, y^n denotes the approximation of a time–dependent function y at time level t^n, and $y^{n+\theta_n} = \theta_n y^{n+1} + (1 - \theta_n) y^n$. We note that (3.1) differs from the classical linear multistep $\theta-$method [30]. As shown in [17], problem (3.1) can be solved in a BE–FE fashion as

$$\text{BE:} \quad \frac{y^{n+\theta_n} - y^n}{\theta_n \tau_n} = f(t^{n+\theta_n}, y^{n+\theta_n}), \tag{3.2}$$

$$\text{FE:} \quad \frac{y^{n+1} - y^{n+\theta_n}}{(1 - \theta_n)\tau_n} = f(t^{n+\theta_n}, y^{n+\theta_n}). \tag{3.3}$$

Using the first equation in the second equation, the FE problem can also be written as a linear extrapolation (which acts as post–processing), given by

$$y^{n+1} = \frac{1}{\theta_n} y^{n+\theta_n} - \left(\frac{1}{\theta_n} - 1\right) y^n.$$

We note that when $\theta = \frac{1}{2}$, problem (3.2)-(3.3) is equivalent to the midpoint rule [19, 22, 23, 29, 31], hence conserving all quadratic Hamiltonians (e.g., mass and energy) [2,10]. Therefore, in that case, (3.2)-(3.3) is an implicit, conservative, second–order B–stable time–stepping method. The scheme remains unconditionally B–stable for $\theta \in [\frac{1}{2}, 1]$.

We start by rewriting the coupled FSI problem. Introducing the displacement velocity $\boldsymbol{\xi} = \partial_t \boldsymbol{\eta}$, the coupled problem can be reformulated in the following way: Find $\boldsymbol{u}, p, \boldsymbol{\eta}$ and $\boldsymbol{\xi}$ such that

$$\rho_f \partial_t \boldsymbol{u} = \nabla \cdot \boldsymbol{\sigma}(\boldsymbol{u}, p) \qquad \text{in } \Omega \times (0, T), \tag{3.4a}$$

$$\nabla \cdot \boldsymbol{u} = 0 \qquad \text{in } \Omega \times (0, T), \tag{3.4b}$$

$$\rho_s h \partial_t \boldsymbol{\xi} + \mathcal{L}_s \boldsymbol{\eta} = -\boldsymbol{\sigma}(\boldsymbol{u}, p)\boldsymbol{n} \qquad \text{on } \Gamma \times (0, T), \tag{3.4c}$$

$$\boldsymbol{u} = \boldsymbol{\xi} = \partial_t \boldsymbol{\eta} \qquad \text{on } \Gamma \times (0, T), \tag{3.4d}$$

with the boundary and initial conditions specified in the previous section. Following the approach in [12,13], we add and subtract the fluid stress in (3.4c), evaluated at the previous time step. Using the operator–splitting, we separate the structure equation in two parts. One part is used to approximate the structure elastodynamics, while the other part is used as a Robin boundary condition in the fluid problem. The partitioned method is then combined with the refactorized Cauchy's one–legged 'θ–like' method (3.2)-(3.3). The proposed numerical scheme is given as follows.

ALGORITHM 1. *Let τ^n be the variable time step and $t^{n+\theta} = t^n + \theta_n \tau^n$, for any $\theta_n \in [\frac{1}{2}, 1]$, and for all $n \ge 0$. Given $\boldsymbol{u}^0$ in Ω, and $\boldsymbol{\eta}^0, \boldsymbol{\xi}^0 = \boldsymbol{u}|_\Gamma^0$ on Γ, we first need to compute $p^{\theta^0}, p^{1+\theta^1}, \boldsymbol{u}^1, \boldsymbol{u}^2$ in Ω, and $\boldsymbol{\eta}^1, \boldsymbol{\eta}^2, \boldsymbol{\xi}^1, \boldsymbol{\xi}^2$ on Γ with a second–order method. A monolithic method or one of the loosely coupled method proposed in [15, 43] could be used, among others. Then for all $n \ge 2$ compute the following:*

STEP 1. *Set the initial guesses as the linearly extrapolated values:*

$$\boldsymbol{\eta}_{(0)}^{n+\theta_n} = \left(1 + \frac{\theta_n \tau^n}{\tau^{n-1}}\right)\boldsymbol{\eta}^n - \frac{\theta_n \tau^n}{\tau^{n-1}} \boldsymbol{\eta}^{n-1},$$

and similarly for $\boldsymbol{\xi}_{(0)}^{n+\theta_n}, \boldsymbol{u}_{(0)}^{n+\theta_n}$. *The pressure initial guess is defined as*

$$p_{(0)}^{n+\theta_n} = \frac{1+\theta_n\tau^n+\tau^{n-1}-\theta_{n-2}\tau^{n-2}}{1+\theta_{n-1}\tau^{n-1}-\theta_{n-2}\tau^{n-2}} p^{n-1+\theta_{n-1}} - \frac{(1-\theta_{n-1})\tau^{n-1}+\theta_n\tau^n}{1+\theta_{n-1}\tau^{n-1}-\theta_{n-2}\tau^{n-2}} p^{n-2+\theta_{n-2}}.$$

For $\kappa \geq 0$, *compute until convergence the* ***backward Euler*** *partitioned problem:*

$$\text{Solid:}\begin{cases} \dfrac{\boldsymbol{\eta}_{(\kappa+1)}^{n+\theta_n}-\boldsymbol{\eta}^n}{\theta_n\tau^n} = \boldsymbol{\xi}_{(\kappa+1)}^{n+\theta_n} & \text{on } \Gamma, \quad (3.5a)\\ \rho_s h\dfrac{\boldsymbol{\xi}_{(\kappa+1)}^{n+\theta_n}-\boldsymbol{\xi}^n}{\theta_n\tau^n} + \mathcal{L}_s\boldsymbol{\eta}_{(\kappa+1)}^{n+\theta_n} = -\boldsymbol{\sigma}(\boldsymbol{u}_{(\kappa)}^{n+\theta_n}, p_{(\kappa)}^{n+\theta_n})\boldsymbol{n} & \text{on } \Gamma, \quad (3.5b)\\ \boldsymbol{\eta}_{(\kappa+1)}^{n+\theta_n} = 0 & \text{on } \partial\Gamma, \quad (3.5c)\end{cases}$$

$$\text{Fluid:}\begin{cases} \rho_f\dfrac{\boldsymbol{u}_{(\kappa+1)}^{n+\theta_n}-\boldsymbol{u}^n}{\theta_n\tau^n} - \nabla\cdot\boldsymbol{\sigma}(\boldsymbol{u}_{(\kappa+1)}^{n+\theta_n}, p_{(\kappa+1)}^{n+\theta_n}) = \boldsymbol{f}_f(t^{n+\theta_n}) & \text{in } \Omega, \quad (3.6a)\\ \nabla\cdot\boldsymbol{u}_{(\kappa+1)}^{n+\theta_n} = 0 & \text{in } \Omega, \quad (3.6b)\\ \rho_s h\dfrac{\boldsymbol{u}_{(\kappa+1)}^{n+\theta_n}-\boldsymbol{\xi}_{(\kappa+1)}^{n+\theta_n}}{\theta_n\tau^n} = -\boldsymbol{\sigma}(\boldsymbol{u}_{(\kappa+1)}^{n+\theta_n}, p_{(\kappa+1)}^{n+\theta_n})\boldsymbol{n} + \boldsymbol{\sigma}(\boldsymbol{u}_{(\kappa)}^{n+\theta_n}, p_{(\kappa)}^{n+\theta_n})\boldsymbol{n} & \text{on } \Gamma. \quad (3.6c)\\ \boldsymbol{\sigma}(\boldsymbol{u}_{(\kappa+1)}^{n+\theta_n}, p_{(\kappa+1)}^{n+\theta_n})\boldsymbol{n} = -p_{in}(t^{n+\theta_n})\boldsymbol{n} & \text{on } \Gamma_{in}, \quad (3.6d)\\ \boldsymbol{\sigma}(\boldsymbol{u}_{(\kappa+1)}^{n+\theta_n}, p_{(\kappa+1)}^{n+\theta_n})\boldsymbol{n} = -p_{out}(t^{n+\theta_n})\boldsymbol{n} & \text{on } \Gamma_{out}. \quad (3.6e)\end{cases}$$

The converged solutions

$$\boldsymbol{\eta}_{(\kappa)}^{n+\theta_n}, \boldsymbol{\xi}_{(\kappa)}^{n+\theta_n}, \boldsymbol{u}_{(\kappa)}^{n+\theta_n}, p_{(\kappa)}^{n+\theta_n} \xrightarrow{\kappa\to\infty} \boldsymbol{\eta}^{n+\theta_n}, \boldsymbol{\xi}^{n+\theta_n}, \boldsymbol{u}^{n+\theta_n}, p^{n+\theta_n},$$

then satisfy:

$$\text{Solid:}\begin{cases} \dfrac{\boldsymbol{\eta}^{n+\theta_n}-\boldsymbol{\eta}^n}{\theta_n\tau^n} = \boldsymbol{\xi}^{n+\theta_n} & \text{on } \Gamma, \quad (3.7a)\\ \rho_s h\dfrac{\boldsymbol{\xi}^{n+\theta_n}-\boldsymbol{\xi}^n}{\theta_n\tau^n} + \mathcal{L}_s\boldsymbol{\eta}^{n+\theta_n} = -\boldsymbol{\sigma}(\boldsymbol{u}^{n+\theta_n}, p^{n+\theta_n})\boldsymbol{n} & \text{on } \Gamma, \quad (3.7b)\\ \boldsymbol{\eta}^{n+\theta_n} = 0 & \text{on } \partial\Gamma, \quad (3.7c)\end{cases}$$

$$\text{Fluid:}\begin{cases} \rho_f\dfrac{\boldsymbol{u}^{n+\theta_n}-\boldsymbol{u}^n}{\theta_n\tau^n} - \nabla\cdot\boldsymbol{\sigma}(\boldsymbol{u}^{n+\theta_n}, p^{n+\theta_n}) = \boldsymbol{f}_f(t^{n+\theta_n}) & \text{in } \Omega, \quad (3.8a)\\ \nabla\cdot\boldsymbol{u}^{n+\theta_n} = 0 & \text{in } \Omega, \quad (3.8b)\\ \boldsymbol{u}^{n+\theta_n} = \boldsymbol{\xi}^{n+\theta_n} & \text{on } \Gamma. \quad (3.8c)\\ \boldsymbol{\sigma}(\boldsymbol{u}^{n+\theta_n}, p^{n+\theta_n})\boldsymbol{n} = -p_{in}(t^{n+\theta_n})\boldsymbol{n} & \text{on } \Gamma_{in}, \quad (3.8d)\\ \boldsymbol{\sigma}(\boldsymbol{u}^{n+\theta_n}, p^{n+\theta_n})\boldsymbol{n} = -p_{out}(t^{n+\theta_n})\boldsymbol{n} & \text{on } \Gamma_{out}. \quad (3.8e)\end{cases}$$

Step 2. *Now evaluate the following (equivalent to solving* ***forward Euler*** *problems):*

$$\text{Solid:}\begin{cases} \boldsymbol{\eta}^{n+1} = \dfrac{1}{\theta_n}\boldsymbol{\eta}^{n+\theta_n} - \dfrac{1-\theta_n}{\theta_n}\boldsymbol{\eta}^n & \text{on } \Gamma, \quad (3.9a)\\ \boldsymbol{\xi}^{n+1} = \dfrac{1}{\theta_n}\boldsymbol{\xi}^{n+\theta_n} - \dfrac{1-\theta_n}{\theta_n}\boldsymbol{\xi}^n & \text{on } \Gamma, \quad (3.9b)\end{cases}$$

$$\text{Fluid:}\begin{cases} \boldsymbol{u}^{n+1} = \dfrac{1}{\theta_n}\boldsymbol{u}^{n+\theta_n} - \dfrac{1-\theta_n}{\theta_n}\boldsymbol{u}^{n} & \text{in } \Omega. \end{cases} \tag{3.10}$$

STEP 3. *Compute the local truncation error, $\hat{T}^{n+1}$, and given a tolerance, δ, adapt the time step:*

$$\tau^{new} = \tau^n \min\left\{ r_{max}, \max\left\{ r_{min}, s\left(\frac{\delta}{\|\hat{T}^{n+1}\|}\right)^{\frac{1}{3}} \right\} \right\}. \tag{3.11}$$

If $\|\hat{T}^{n+1}\| \le \delta$, set $\tau^{n+1} = \tau^{new}$, chose $\theta_{n+1} \in [\frac{1}{2}, 1]$, and evolve the time interval $t^{n+2} = t^{n+1} + \theta_{n+1}\tau^{n+1}$. Otherwise, set $\tau^n = \tau^{new}$ and go back to Step 1.

REMARK 3.1. *Numbers r_{min} and r_{max} in (3.11) are chosen so that the ratio of τ^{new} and τ^n stays between these values. This type of restriction guarantees the zero–stability of general one–leg variable step size methods (see e.g., [21, 28, 34, 36, 37]), and helps to keep the time step from changing too rapidly, which is especially important in stiff problems. The coefficient $s \in [\frac{1}{2}, 1)$ is a 'safety' parameter, routinely used to reduce the number of rejected time steps in the adaptive algorithm.*

REMARK 3.2. *We note that for $\theta_n = 1/2 + \mathcal{O}(\tau^n)$ the method is second-order accurate.*

REMARK 3.3. *We also note that the linear extrapolations in (3.9)-(3.10) can be written as forward Euler problems. While linear extrapolations are more desirable from the implementational point of view, in stability analysis we will use their forward Euler formulation, given as follows*

$$\text{Solid:}\begin{cases} \dfrac{\boldsymbol{\eta}^{n+1} - \boldsymbol{\eta}^{n+\theta_n}}{(1-\theta_n)\tau^n} = \boldsymbol{\xi}^{n+\theta_n} & \text{on } \Gamma, \quad (3.12a) \\ \rho_s h \dfrac{\boldsymbol{\xi}^{n+1} - \boldsymbol{\xi}^{n+\theta_n}}{(1-\theta_n)\tau^n} + \mathcal{L}_s \boldsymbol{\eta}^{n+\theta_n} = -\boldsymbol{\sigma}(\boldsymbol{u}^{n+\theta_n}, p^{n+\theta_n})\boldsymbol{n} & \text{in } \Gamma, \quad (3.12b) \end{cases}$$

$$\text{Fluid:}\begin{cases} \rho_f \dfrac{\boldsymbol{u}^{n+1} - \boldsymbol{u}^{n+\theta_n}}{(1-\theta_n)\tau^n} - \nabla\cdot\boldsymbol{\sigma}(\boldsymbol{u}^{n+\theta_n}, p^{n+\theta_n}) = \boldsymbol{f}_F(t^{n+\theta_n}). & \text{in } \Omega. \end{cases} \tag{3.13a}$$

3.1. Convergence of the partitioned iterative scheme . In the following, we will use the polarized identity, given by

$$2(a-c)b = a^2 - c^2 - (a-b)^2 + (b-c)^2. \tag{3.14}$$

THEOREM 3.1. *The sequences $\boldsymbol{u}^{n+\theta_n}_{(\kappa)}, \boldsymbol{\eta}^{n+\theta_n}_{(\kappa)}, \boldsymbol{\xi}^{n+\theta_n}_{(\kappa)}$ generated by iterations (3.5)-(3.6) converge as $\kappa \to \infty$:*

$$\begin{aligned} &\boldsymbol{u}^{n+\theta_n}_{(\kappa)} \longrightarrow \boldsymbol{u}^{n+\theta_n} \quad \text{in } H^1(\Omega)\cap L^2(\Gamma), \\ &\boldsymbol{\eta}^{n+\theta_n}_{(\kappa)} \longrightarrow \boldsymbol{\eta}^{n+\theta_n} \quad \text{in } H^1(\Gamma), \qquad \boldsymbol{\xi}^{n+\theta_n}_{(\kappa)} \longrightarrow \boldsymbol{\xi}^{n+\theta_n} \quad \text{in } L^2(\Gamma). \end{aligned}$$

Proof. We begin by subtracting (3.5)-(3.6) from the equations (3.7)-(3.8). Using notation

$$\begin{aligned} &\boldsymbol{\delta}^{\eta}_{\kappa+1} = \boldsymbol{\eta}^{n+\theta_n} - \boldsymbol{\eta}^{n+\theta_n}_{(\kappa+1)}, \quad \boldsymbol{\delta}^{\xi}_{\kappa+1} = \boldsymbol{\xi}^{n+\theta_n} - \boldsymbol{\xi}^{n+\theta_n}_{(\kappa+1)}, \\ &\boldsymbol{\delta}^{u}_{\kappa+1} = \boldsymbol{u}^{n+\theta_n} - \boldsymbol{u}^{n+\theta_n}_{(\kappa+1)}, \quad \delta^{p}_{\kappa+1} = p^{n+\theta_n} - p^{n+\theta_n}_{(\kappa+1)}, \end{aligned}$$

we obtain the following:

$$\text{Solid:}\begin{cases} \dfrac{\boldsymbol{\delta}^{\eta}_{\kappa+1}}{\theta_n\tau^n} = \boldsymbol{\delta}^{\xi}_{\kappa+1} & \text{on } \Gamma, \quad (3.15a) \\ \rho_s h \dfrac{\boldsymbol{\delta}^{\xi}_{\kappa+1}}{\theta_n\tau^n} + \mathcal{L}_s\left(\boldsymbol{\delta}^{\eta}_{\kappa+1}\right) = -\boldsymbol{\sigma}(\boldsymbol{\delta}^{u}_{\kappa}, p^{n+\theta_n}_{(\kappa)})\boldsymbol{n} & \text{on } \Gamma, \quad (3.15b) \end{cases}$$

$$\text{Fluid:}\begin{cases} \rho_f \dfrac{\boldsymbol{\delta}^u_{\kappa+1}}{\theta_n\tau^n} - \nabla\cdot\boldsymbol{\sigma}(\boldsymbol{\delta}^u_{\kappa+1},\delta^p_{\kappa+1}) = 0 & \text{in } \Omega, \qquad (3.16a)\\ \nabla\cdot\boldsymbol{\delta}^u_{\kappa+1} = 0 & \text{in } \Omega, \qquad (3.16b)\\ \rho_s h\dfrac{\boldsymbol{\delta}^u_{\kappa+1}-\boldsymbol{\delta}^\xi_{\kappa+1}}{\theta_n\tau^n} = \boldsymbol{\sigma}(\boldsymbol{\delta}^u_{\kappa},\delta^p_{\kappa})\boldsymbol{n} - \boldsymbol{\sigma}(\boldsymbol{\delta}^u_{\kappa+1},\delta^p_{\kappa+1})\boldsymbol{n} & \text{on } \Gamma. \qquad (3.16c)\end{cases}$$

We note that in this case, the structure equations (3.15) are complemented with homogeneous Dirichlet boundary conditions (2.2b), and the fluid equations (3.16) are complemented with the homogeneous Neumann boundary conditions. We multiply (3.15a) by $\mathcal{L}_s(\boldsymbol{\delta}^\eta_{\kappa+1})$ and (3.15b) by $\boldsymbol{\delta}^\xi_{\kappa+1}$, integrate over Γ, and add to obtain

$$0 = \frac{1}{\theta_n\tau^n}\|\boldsymbol{\delta}^\eta_{\kappa+1}\|^2_S + \frac{\rho_s h}{\theta_n\tau^n}\|\boldsymbol{\delta}^\xi_{\kappa+1}\|^2_{L^2(\Gamma)} + \int_\Gamma \boldsymbol{\sigma}(\boldsymbol{\delta}^u_{\kappa},\delta^p_{\kappa})\boldsymbol{n}\cdot\boldsymbol{\delta}^\xi_{\kappa+1}.$$

For the fluid part, we multiply (3.16a) by $\boldsymbol{\delta}^u_{\kappa+1}$ and (3.16b) by $\delta^p_{\kappa+1}$. Integrating over Ω, and using (3.16c) and the polarized identity (3.14), we obtain

$$\begin{aligned} 0 = {} & \frac{\rho_f}{\theta_n\tau^n}\|\boldsymbol{\delta}^u_{\kappa+1}\|^2_{L^2(\Omega)} + 2\mu\|\boldsymbol{D}(\boldsymbol{\delta}^u_{\kappa+1})\|^2_{L^2(\Omega)} + \frac{\rho_s h}{2\theta_n\tau^n}\left(\|\boldsymbol{\delta}^u_{\kappa+1}\|^2_{L^2(\Gamma)} - \|\boldsymbol{\delta}^\xi_{\kappa+1}\|^2_{L^2(\Gamma)}\right)\\ & + \frac{\rho_s h}{2\theta_n\tau^n}\|\boldsymbol{\delta}^u_{\kappa+1}-\boldsymbol{\delta}^\xi_{\kappa+1}\|^2_{L^2(\Gamma)} - \int_\Gamma \boldsymbol{\sigma}(\boldsymbol{\delta}^u_{\kappa},\delta^p_{\kappa})\boldsymbol{n}\cdot\boldsymbol{\delta}^u_{\kappa+1}.\end{aligned}$$

Therefore, the structure and fluid estimates combine to give

$$\begin{aligned} 0 = {} & \frac{1}{\theta_n\tau^n}\|\boldsymbol{\delta}^\eta_{\kappa+1}\|^2_S + \frac{\rho_f}{\theta_n\tau^n}\|\boldsymbol{\delta}^u_{\kappa+1}\|^2_{L^2(\Omega)} + 2\mu\|\boldsymbol{D}(\boldsymbol{\delta}^u_{\kappa+1})\|^2_{L^2(\Omega)} + \frac{\rho_s h}{2\theta_n\tau^n}\left(\|\boldsymbol{\delta}^u_{\kappa+1}\|^2_{L^2(\Gamma)} + \|\boldsymbol{\delta}^\xi_{\kappa+1}\|^2_{L^2(\Gamma)}\right)\\ & + \frac{\rho_s h}{2\theta_n\tau^n}\|\boldsymbol{\delta}^u_{\kappa+1}-\boldsymbol{\delta}^\xi_{\kappa+1}\|^2_{L^2(\Gamma)} + \int_\Gamma \boldsymbol{\sigma}(\boldsymbol{\delta}^u_{\kappa},\delta^p_{\kappa})\boldsymbol{n}\cdot(\boldsymbol{\delta}^\xi_{\kappa+1}-\boldsymbol{\delta}^u_{\kappa+1}).\end{aligned}$$

Using again the boundary condition (3.16c) and the polarized identity (3.14), we have that

$$\begin{aligned} & \int_\Gamma \boldsymbol{\sigma}(\boldsymbol{\delta}^u_{\kappa},\delta^p_{\kappa})\boldsymbol{n}\cdot(\boldsymbol{\delta}^\xi_{\kappa+1}-\boldsymbol{\delta}^u_{\kappa+1})\\ & = \frac{\theta_n\tau^n}{2\rho_s h}\left(\left\|\boldsymbol{\sigma}(\boldsymbol{\delta}^u_{\kappa+1},\delta^p_{\kappa+1})\boldsymbol{n}\right\|^2_{L^2(\Gamma)} - \|\boldsymbol{\sigma}(\boldsymbol{\delta}^u_{\kappa},\delta^p_{\kappa})\boldsymbol{n}\|^2_{L^2(\Gamma)}\right) - \frac{\rho_s h}{2\theta_n\tau^n}\left\|\boldsymbol{\delta}^\xi_{\kappa+1}-\boldsymbol{\delta}^u_{\kappa+1}\right\|^2_{L^2(\Gamma)},\end{aligned}$$

and therefore,

$$\begin{aligned} 0 = {} & \frac{1}{\theta_n\tau^n}\|\boldsymbol{\delta}^\eta_{\kappa+1}\|^2_S + \frac{\rho_f}{\theta_n\tau^n}\|\boldsymbol{\delta}^u_{\kappa+1}\|^2_{L^2(\Omega)} + 2\mu\|\boldsymbol{D}(\boldsymbol{\delta}^u_{\kappa+1})\|^2_{L^2(\Omega)} + \frac{\rho_s h}{2\theta_n\tau^n}\left(\|\boldsymbol{\delta}^u_{\kappa+1}\|^2_{L^2(\Gamma)} + \|\boldsymbol{\delta}^\xi_{\kappa+1}\|^2_{L^2(\Gamma)}\right)\\ & + \frac{\theta_n\tau^n}{2\rho_s h}\left(\left\|\boldsymbol{\sigma}(\boldsymbol{\delta}^u_{\kappa+1},\delta^p_{\kappa+1})\boldsymbol{n}\right\|^2_{L^2(\Gamma)} - \|\boldsymbol{\sigma}(\boldsymbol{\delta}^u_{\kappa},\delta^p_{\kappa})\boldsymbol{n}\|^2_{L^2(\Gamma)}\right).\end{aligned}$$

Equivalently this can be written as

$$\begin{aligned} & \|\boldsymbol{\delta}^\eta_{\kappa+1}\|^2_S + \rho_f\|\boldsymbol{\delta}^u_{\kappa+1}\|^2_{L^2(\Omega)} + 2\mu\theta_n\tau^n\|\boldsymbol{D}(\boldsymbol{\delta}^u_{\kappa+1})\|^2_{L^2(\Omega)} + \frac{\rho_s h}{2}\left(\|\boldsymbol{\delta}^u_{\kappa+1}\|^2_{L^2(\Gamma)} + \|\boldsymbol{\delta}^\xi_{\kappa+1}\|^2_{L^2(\Gamma)}\right)\\ & + \frac{|\theta_n\tau^n|^2}{2\rho_s h}\left\|\boldsymbol{\sigma}(\boldsymbol{\delta}^u_{\kappa+1},\delta^p_{\kappa+1})\boldsymbol{n}\right\|^2_{L^2(\Gamma)} = \frac{|\theta_n\tau^n|^2}{2\rho_s h}\|\boldsymbol{\sigma}(\boldsymbol{\delta}^u_{\kappa},\delta^p_{\kappa})\boldsymbol{n}\|^2_{L^2(\Gamma)},\end{aligned}$$

which yields that, as $\kappa \nearrow \infty$, the sequences of iterations $\boldsymbol{u}^{n+\theta_n}_{(\kappa)}$, $\boldsymbol{\eta}^{n+\theta_n}_{(\kappa)}$, $\boldsymbol{\xi}^{n+\theta_n}_{(\kappa)}$ converge linearly to $\boldsymbol{u}^{n+\theta_n}, \boldsymbol{\eta}^{n+\theta_n}, \boldsymbol{\xi}^{n+\theta_n}$, respectively, in the strong topologies of $H^1(\Omega)\cap L^2(\Gamma), H^1(\Gamma)$ and $L^2(\Gamma)$. □

3.2. Stability – energy estimates. Denote by $\mathcal{E}^N$ is the sum of the elastic energy of the structure, kinetic energy of the structure and kinetic energy of the fluid

$$\mathcal{E}^N = \frac{1}{2}\|\boldsymbol{\eta}^N\|_S^2 + \frac{\rho_s h}{2}\|\boldsymbol{\xi}^N\|_{L^2(\Gamma)}^2 + \frac{\rho_f}{2}\|\boldsymbol{u}^N\|_{L^2(\Omega)}^2,$$

and by $\mathcal{D}^N$ the fluid viscous dissipation rate

$$\mathcal{D}^N = 2\mu \sum_{n=2}^{N-1} \tau^n \|\boldsymbol{D}(\boldsymbol{u}^{n+\theta_n})\|_{L^2(\Omega)}^2.$$

The stability of the scheme presented in Algorithm 1 is given in the following theorem.

THEOREM 3.2. *Let $\{(\boldsymbol{\xi}^n, \boldsymbol{\eta}^n, \boldsymbol{u}^n, p^n)\}_{2\le n\le N}$ be the solution of Algorithm 1, assuming that the system is isolated, i.e., $\boldsymbol{f}_f = 0, p_{in} = 0$ and $p_{out} = 0$. Then, for $\theta_n \ge \frac{1}{2}$, the method is unconditionally energy stable, and the following a priori energy equality holds*

$$\mathcal{E}^N + \mathcal{D}^N + \mathcal{N}^N = \mathcal{E}^2,$$

where $\mathcal{N}^N$ denotes the numerical dissipation

$$\mathcal{N}^N = \sum_{n=2}^{N-1} \frac{(\tau^n)^2(2\theta_n - 1)}{2}\|\boldsymbol{\xi}^{n+\theta_n}\|_S^2 + \frac{\rho_s h}{2}\sum_{n=2}^{N-1}(2\theta_n - 1)\|\boldsymbol{\xi}^{n+1} - \boldsymbol{\xi}^n\|_{L^2(\Gamma)}^2 + \frac{\rho_f}{2}\sum_{n=2}^{N-1}(2\theta_n - 1)\|\boldsymbol{u}^{n+1} - \boldsymbol{u}^n\|_{L^2(\Omega)}^2.$$

Proof. We multiply (3.7a) by $\theta_n \mathcal{L}_s \boldsymbol{\eta}^{n+\theta_n}$ and (3.7b) by $\theta_n \boldsymbol{\xi}^{n+\theta_n}$, integrate over Γ, add and apply (3.14) to obtain

$$0 = \frac{1}{2\tau^n}\Big(\|\boldsymbol{\eta}^{n+\theta_n}\|_S^2 - \|\boldsymbol{\eta}^n\|_S^2 + \|\boldsymbol{\eta}^{n+\theta_n} - \boldsymbol{\eta}^n\|_S^2\Big) + \frac{\rho_s h}{2\tau^n}\Big(\|\boldsymbol{\xi}^{n+\theta_n}\|_{L^2(\Gamma)}^2 - \|\boldsymbol{\xi}^n\|_{L^2(\Gamma)}^2 + \|\boldsymbol{\xi}^{n+\theta_n} - \boldsymbol{\xi}^n\|_{L^2(\Gamma)}^2\Big) + \theta_n \int_\Gamma \boldsymbol{\sigma}(\boldsymbol{u}^{n+\theta_n}, p^{n+\theta_n})\boldsymbol{n}\cdot\boldsymbol{\xi}^{n+\theta_n}.$$

Similarly, multiplying (3.12a) by $(1-\theta_n)\mathcal{L}_s\boldsymbol{\eta}^{n+\theta_n}$ and (3.12b) by $(1-\theta_n)\boldsymbol{\xi}^{n+\theta_n}$, we derive

$$0 = \frac{1}{2\tau^n}\Big(\|\boldsymbol{\eta}^{n+1}\|_S^2 - \|\boldsymbol{\eta}^{n+\theta_n}\|_S^2 - \|\boldsymbol{\eta}^{n+1} - \boldsymbol{\eta}^{n+\theta_n}\|_S^2\Big) + \frac{\rho_s h}{2\tau^n}\Big(\|\boldsymbol{\xi}^{n+1}\|_{L^2(\Gamma)}^2 - \|\boldsymbol{\xi}^{n+\theta_n}\|_{L^2(\Gamma)}^2 - \|\boldsymbol{\xi}^{n+1} - \boldsymbol{\xi}^{n+\theta_n}\|_{L^2(\Gamma)}^2\Big) + (1-\theta_n)\int_\Gamma \boldsymbol{\sigma}(\boldsymbol{u}^{n+\theta_n}, p^{n+\theta_n})\boldsymbol{n}\cdot\boldsymbol{\xi}^{n+\theta_n}.$$

Hence, from the structure part, we have

$$0 = \frac{1}{2\tau^n}\Big(\|\boldsymbol{\eta}^{n+1}\|_S^2 - \|\boldsymbol{\eta}^n\|_S^2 - \|\boldsymbol{\eta}^{n+1} - \boldsymbol{\eta}^{n+\theta_n}\|_S^2 + \|\boldsymbol{\eta}^{n+\theta_n} - \boldsymbol{\eta}^n\|_S^2\Big) + \frac{\rho_s h}{2\tau^n}\Big(\|\boldsymbol{\xi}^{n+1}\|_{L^2(\Gamma)}^2 - \|\boldsymbol{\xi}^n\|_{L^2(\Gamma)}^2 - \|\boldsymbol{\xi}^{n+1} - \boldsymbol{\xi}^{n+\theta_n}\|_{L^2(\Gamma)}^2 + \|\boldsymbol{\xi}^{n+\theta_n} - \boldsymbol{\xi}^n\|_{L^2(\Gamma)}^2\Big) + \int_\Gamma \boldsymbol{\sigma}(\boldsymbol{u}^{n+\theta_n}, p^{n+\theta_n})\boldsymbol{n}\cdot\boldsymbol{\xi}^{n+\theta_n}.$$

Using again the displacement equations (3.12a) and (3.7a), we have

$$-\|\boldsymbol{\eta}^{n+1} - \boldsymbol{\eta}^{n+\theta_n}\|_S^2 + \|\boldsymbol{\eta}^{n+\theta_n} - \boldsymbol{\eta}^n\|_S^2 = (\tau^n)^2(2\theta_n - 1)\|\boldsymbol{\xi}^{n+\theta_n}\|_S^2,$$

while the velocity equation (3.9b) yields

$$-\|\boldsymbol{\xi}^{n+1}-\boldsymbol{\xi}^{n+\theta_n}\|^2_{L^2(\Gamma)}+\|\boldsymbol{\xi}^{n+\theta_n}-\boldsymbol{\xi}^{n}\|^2_{L^2(\Gamma)}=(2\theta_n-1)\|\boldsymbol{\xi}^{n+1}-\boldsymbol{\xi}^{n}\|^2_{L^2(\Gamma)}.$$

Hence the energy estimate of the structure part gives

$$\begin{aligned}0=&\frac{1}{2\tau^n}\big(\|\boldsymbol{\eta}^{n+1}\|^2_S-\|\boldsymbol{\eta}^{n}\|^2_S\big)+\frac{\rho_s h}{2\tau^n}\big(\|\boldsymbol{\xi}^{n+1}\|^2_{L^2(\Gamma)}-\|\boldsymbol{\xi}^{n}\|^2_{L^2(\Gamma)}\big)+\frac{\tau^n(2\theta_n-1)}{2}\|\boldsymbol{\xi}^{n+\theta_n}\|^2_S\\&+\frac{\rho_s h(2\theta_n-1)}{2\tau^n}\|\boldsymbol{\xi}^{n+1}-\boldsymbol{\xi}^{n}\|^2_{L^2(\Gamma)}+\int_\Gamma\boldsymbol{\sigma}(\boldsymbol{u}^{n+\theta_n},p^{n+\theta_n})\boldsymbol{n}\cdot\boldsymbol{\xi}^{n+\theta_n}.\end{aligned}\tag{3.17}$$

For the fluid part, we multiply (3.8a) by $\theta_n\boldsymbol{u}^{n+\theta_n}$ and (3.8b) by $\theta_n p^{n+\frac{1}{2}}$. Integrating over Ω, adding, and using (3.8c) and the homogeneous Neumann boundary conditions, we obtain

$$\begin{aligned}0=&\frac{\rho_f}{2\tau^n}\Big(\|\boldsymbol{u}^{n+1}\|^2_{L^2(\Omega)}-\|\boldsymbol{u}^{n}\|^2_{L^2(\Omega)}-\|\boldsymbol{u}^{n+1}-\boldsymbol{u}^{n+\theta_n}\|^2_{L^2(\Omega)}+\|\boldsymbol{u}^{n+\theta_n}-\boldsymbol{u}^{n}\|^2_{L^2(\Omega)}\Big)\\&+2\mu\|\boldsymbol{D}(\boldsymbol{u}^{n+\theta_n})\|^2_{L^2(\Omega)}-\int_\Gamma\boldsymbol{\sigma}(\boldsymbol{u}^{n+\theta_n},p^{n+\theta_n})\boldsymbol{n}\cdot\boldsymbol{\xi}^{n+\theta_n}.\end{aligned}$$

Taking into account the flow equation (3.10), we have

$$-\|\boldsymbol{u}^{n+1}-\boldsymbol{u}^{n+\theta_n}\|^2_{L^2(\Omega)}+\|\boldsymbol{u}^{n+\theta_n}-\boldsymbol{u}^{n}\|^2_{L^2(\Omega)}=(2\theta_n-1)\|\boldsymbol{u}^{n+1}-\boldsymbol{u}^{n}\|^2_{L^2(\Omega)}.$$

Hence, the fluid part of the energy estimates gives

$$\begin{aligned}0=&\frac{\rho_f}{2\tau^n}\big(\|\boldsymbol{u}^{n+1}\|^2_{L^2(\Omega)}-\|\boldsymbol{u}^{n}\|^2_{L^2(\Omega)}\big)+\frac{\rho_f(2\theta_n-1)}{2\tau^n}\|\boldsymbol{u}^{n+1}-\boldsymbol{u}^{n}\|^2_{L^2(\Omega)}+2\mu\|\boldsymbol{D}(\boldsymbol{u}^{n+\theta_n})\|^2_{L^2(\Omega)}\\&-\int_\Gamma\boldsymbol{\sigma}(\boldsymbol{u}^{n+\theta_n},p^{n+\theta_n})\boldsymbol{n}\cdot\boldsymbol{\xi}^{n+\theta_n}.\end{aligned}\tag{3.18}$$

The structure (3.17) and fluid (3.18) estimates combine to give

$$\begin{aligned}0=&\frac{1}{2\tau^n}\big(\|\boldsymbol{\eta}^{n+1}\|^2_S-\|\boldsymbol{\eta}^{n}\|^2_S\big)+\frac{\rho_s h}{2\tau^n}\big(\|\boldsymbol{\xi}^{n+1}\|^2_{L^2(\Gamma)}-\|\boldsymbol{\xi}^{n}\|^2_{L^2(\Gamma)}\big)+\frac{\tau^n(2\theta_n-1)}{2}\|\boldsymbol{\xi}^{n+\theta_n}\|^2_S\\&+\frac{\rho_s h(2\theta_n-1)}{2\tau^n}\|\boldsymbol{\xi}^{n+1}-\boldsymbol{\xi}^{n}\|^2_{L^2(\Gamma)}+\frac{\rho_f}{2\tau^n}\big(\|\boldsymbol{u}^{n+1}\|^2_{L^2(\Omega)}-\|\boldsymbol{u}^{n}\|^2_{L^2(\Omega)}\big)\\&+\frac{\rho_f(2\theta_n-1)}{2\tau^n}\|\boldsymbol{u}^{n+1}-\boldsymbol{u}^{n}\|^2_{L^2(\Omega)}+2\mu\|\boldsymbol{D}(\boldsymbol{u}^{n+\theta_n})\|^2_{L^2(\Omega)}.\end{aligned}\tag{3.19}$$

Summation from $n=2$ to $N-1$ and multiplication by τ^n yields the desired estimate.
□

REMARK 3.4. *We note that when $\theta_n=\frac{1}{2}$, for all n, we have $\mathcal{N}^N=0$, and the method is conservative.*

COROLLARY 3.3. *Let $\{(\boldsymbol{\xi}^n,\boldsymbol{\eta}^n,\boldsymbol{u}^n,p^n)\}_{2\le n\le N}$ be the solution of Algorithm 1, assuming non–zero volume and boundary forcing. Then, for $\theta_n\ge\frac{1}{2}$, the method is unconditionally energy stable, and the following a priori energy inequality holds*

$$\mathcal{E}^N+\frac{1}{2}\mathcal{D}^N+\mathcal{N}^N\le\mathcal{E}^2+\mathcal{F}^N,$$

where $\mathcal{F}^N$ denotes the forcing terms

$$\mathcal{F}^N=\frac{C_1}{\mu}\|\boldsymbol{f}_f(t^{n+\theta_n})\|^2_{L^2(\Omega)}+\frac{C_2}{\mu}\|p_{in}(t^{n+\theta_n})\|^2_{L^2(\Gamma_{in})}+\frac{C_2}{\mu}\|p_{out}(t^{n+\theta_n})\|^2_{L^2(\Gamma_{out})}.$$

Proof. The main steps of the proof are the same as in Theorem 3.2. We estimate the additional terms due to non–zero volume and boundary forcing as follows. Using the Cauchy-Schwarz, trace, Poincaré and Korn inequalities [16], we have

$$\int_\Omega\boldsymbol{f}_f(t^{n+\theta_n})\cdot\boldsymbol{u}^{n+\theta_n}-\int_{\Gamma_{in}}p_{in}(t^{n+\theta_n})\boldsymbol{u}^{n+\theta_n}\cdot\boldsymbol{n}-\int_{\Gamma_{out}}p_{out}(t^{n+\theta_n})\boldsymbol{u}^{n+\theta_n}\cdot\boldsymbol{n}$$

$$\leq \frac{C_1}{\mu}\|\boldsymbol{f}_f(t^{n+\theta_n})\|^2_{L^2(\Omega)} + \frac{C_2}{\mu}\|p_{in}(t^{n+\theta_n})\|^2_{L^2(\Gamma_{in})} + \frac{C_2}{\mu}\|p_{out}(t^{n+\theta_n})\|^2_{L^2(\Gamma_{out})}$$
$$+ \mu\|\boldsymbol{D}(\boldsymbol{u}^{n+\theta_n})\|^2_{L^2(\Omega)}, \tag{3.20}$$

Combining (3.20) with (3.19), summing from $n = 2$ to $N-1$ and multiplying by τ^n proves the Corollary. ∎

4. Computing the local truncation error. The time step adaptivity can be implemented in numerous ways (see e.g. [32]). In this work, we compute the local truncation error using the difference between the second–order midpoint solution, denoted by $y^{n+1}_{midpoint}$, and a second–order approximation given by a formula similar to the explicit Adams–Bashforth two–step (AB2) method, denoted by y^{n+1}_{AB2}. The difference between this method and the classical AB2 formula is that the function values are evaluated at half–times, as described in [17]. The solution obtained using the AB2 method is computed as

$$y^{n+1}_{AB2} = y^n \frac{(\tau^n+\tau^{n-1})(\tau^n+\tau^{n-1}+\tau^{n-2})}{\tau^{n-1}(\tau^{n-1}+\tau^{n-2})} - y^{n-1}\frac{\tau^n(\tau^n+\tau^{n-1}+\tau^{n-2})}{\tau^{n-1}\tau^{n-2}} + y^{n-2}\frac{\tau^n(\tau^n+\tau^{n-1})}{\tau^{n-2}(\tau^{n-1}+\tau^{n-2})}.$$

The local truncation error for the AB2 method, under localization assumption [32, 38], can be written as

$$T^{n+1}_{AB2} = (\tau^n)^3 y'''(t^{n+\frac{1}{2}})\mathcal{R}^n, \quad \text{where} \quad \mathcal{R}^n = \frac{1}{24} + \frac{1}{8}\left(1+\frac{\tau^{n-1}}{\tau^n}\right)\left(1+2\frac{\tau^{n-1}}{\tau^n}+\frac{\tau^{n-2}}{\tau^n}\right). \tag{4.1}$$

The local truncation error for the midpoint method, as well as the 'θ–like' method for $\theta_n = \frac{1}{2} + \frac{1}{2}(\tau^n)^2$, is given by

$$\hat{T}^{n+1} = \frac{1}{24}(\tau^n)^3 y'''(t^{n+\frac{1}{2}}) + \mathcal{O}((\tau^n)^5).$$

Using (4.1), the local truncation error of the midpoint method can be written as

$$\hat{T}^{n+1} = \left(y^{n+1}_{midpoint} - y^{n+1}_{AB2}\right)\frac{1}{1-1/(24\mathcal{R}^n)}. \tag{4.2}$$

This relation will be used to compute the local truncation error in Step 3 of Algorithm 1.

5. Numerical examples. For spatial discretization of Algorithm 1, we use the finite element method with uniform, conforming meshes. The problem is implemented in the finite element solver FreeFem++ [35]. We investigate the performance of the proposed method in three numerical examples. In the first example, we study the convergence rates of Algorithm 1 when used with a fixed time step on a benchmark problem based on the method of manufactured solutions. We also compare the average number of iterations in the sub-iterative process needed by Algorithm 1 and two other strongly–coupled schemes commonly used in the literature. In the second example, the adaptive time–stepping is applied on the same benchmark problem. Finally, in the third example we consider a benchmark problem describing pressure propagation in a two–dimensional channel commonly used to test FSI solvers, and compare different fixed and the variable time–stepping approaches.

5.1. Example 1. In this example, we assume that the time step is fixed, and study the convergence rates of Algorithm 1. For this purpose, we use the method of manufactured solution. The fluid domain is defined as $\Omega = (-0.5, 0.5) \times (0, 1)$, and $\Gamma = (-0.5, 0.5) \times \{1\}$ represent the structure domain.

We model the structure using the elastic Koiter shell model [12] defined on Γ, accounting for both tangential (horizontal) and transverse (vertical) displacements η_x and η_y, given by

$$\rho_s h\partial_{tt}\eta_x - C_2\partial_x\eta_y - C_3\partial_{xx}\eta_x = f_{s,x}, \tag{5.1}$$
$$\rho_s h\partial_{tt}\eta_y + C_0\eta_y - C_1\partial_{xx}\eta_y + C_2\partial_x\eta_x = f_{s,y}. \tag{5.2}$$

We note that due to the fluid–structure coupling, we have $\boldsymbol{f}_s = -\boldsymbol{\sigma}\boldsymbol{n}$. The exact solutions are given by

$$\boldsymbol{\eta}^{ref} = (\eta^{ref}_x, \eta^{ref}_y)^T = \begin{bmatrix} 10^{-3}e^t\sin(\pi x)\sin(\pi y) \\ -10^{-3}\dfrac{e^t\cos(\pi x)}{\pi(C_2-\mu)}\left(\rho_s h\sin(\pi y) + C_3\pi^2\sin(\pi y) + \mu\pi\cos(\pi y)\right) \end{bmatrix},$$

$$\boldsymbol{u}^{ref} = (u_x^{ref}, u_y^{ref})^T = \begin{bmatrix} 10^{-3} e^t \sin(\pi x)\sin(\pi y) \\ -10^{-3}\dfrac{e^t\cos(\pi x)}{\pi(C_2-\mu)}\left(\rho_s h \sin(\pi y) + C_3\pi^2\sin(\pi y) + \mu\pi\cos(\pi y)\right) \end{bmatrix},$$

$$p^{ref} = (\rho_s h + C_0)u_y^{ref} - C_1\frac{\partial^2 u_y^{ref}}{\partial x^2} + C_2\frac{\partial u_x^{ref}}{\partial x} + 2\mu\frac{\partial u_y^{ref}}{\partial y},$$

using which the forcing term $\boldsymbol{f}_f$ is computed. We note that the exact solutions satisfy the coupling conditions (2.3)-(2.4). Based on the exact solution, we impose Dirichlet boundary conditions on the bottom of the fluid domain, and Neumann boundary conditions on the sides. We also impose homogeneous Dirichlet boundary conditions for the structure. The parameters used in this problem are $\rho_f = \rho_s = h = C_0 = C_1 = C_2 = C_3 = 1$ and $\mu = 0.5$. The problem is solved until the final time $T = 10$ is reached.

To discretize the problem in space, we use $\mathbb{P}_2$ elements for the fluid velocity and solid displacement and velocity, and $\mathbb{P}_1$ elements for the pressure. In order to compute the rates of convergence of our scheme, we first define the errors for the solid displacement and velocity, and fluid velocity, respectively, as follows

$$e_\eta^{ref} = \frac{\|\boldsymbol{\eta} - \boldsymbol{\eta}^{ref}\|_S^2}{\|\boldsymbol{\eta}^{ref}\|_S^2}, \quad e_\xi^{ref} = \frac{\left\|\boldsymbol{\xi} - \boldsymbol{\xi}^{ref}\right\|_{L^2(\Gamma)}}{\left\|\boldsymbol{\xi}^{ref}\right\|_{L^2(\Gamma)}}, \quad e_u^{ref} = \frac{\|\boldsymbol{u} - \boldsymbol{u}^{ref}\|_{L^2(\Omega)}}{\|\boldsymbol{u}^{ref}\|_{L^2(\Omega)}}, \tag{5.3}$$

where

$$\|\boldsymbol{\eta}\|_S^2 = C_2\|\partial_x\eta_x + \eta_y\|_{L^2(\Gamma)}^2 + (C_3 - C_2)\|\partial_x\eta_x\|_{L^2(\Gamma)}^2 + (C_0 - C_2)\|\eta_y\|_{L^2(\Gamma)}^2 + C_1\|\partial_x\eta_y\|_{L^2(\Gamma)}^2.$$

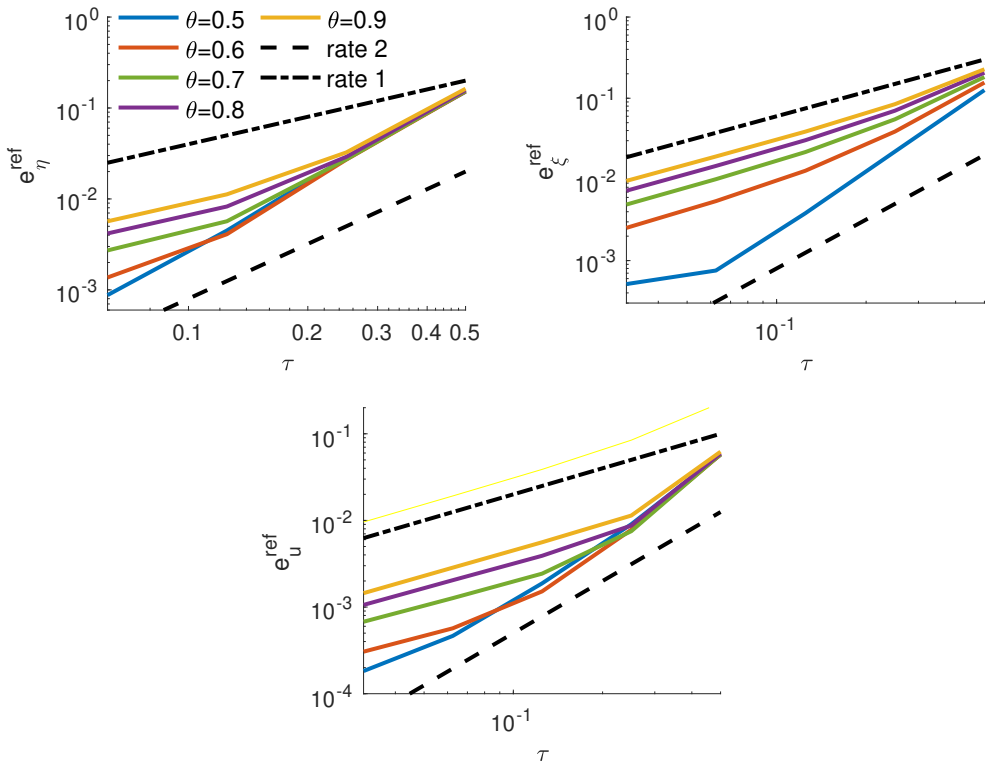

Fig. 5.1: Relative errors for the structure displacement (top–left), structure velocity (top–right), and fluid velocity (bottom) obtained using $\epsilon = 10^{-4}$.

The sub-iterative portion of Algorithm 1, defined by equations (3.5)-(3.6), is computed until the relative errors between two consecutive approximations for the fluid velocity, structure velocity and displacement are less than a given tolerance, ϵ. In the first test, we set $\epsilon = 10^{-4}$ and use the following set of discretization parameters

$$\{\tau, \Delta x\} = \left\{ \frac{0.02}{2^i}, \frac{0.25}{2^i} \right\}_{i=0}^{3},$$

where Δx is the mesh size. Figure 5.1 shows the convergence rates obtained using different values of θ. We note that the second–order convergence is expected when $\theta = \frac{1}{2}$, because in this case the refactorized Cauchy's method corresponds to the midpoint rule. For $\theta = \frac{1}{2}$, we observe a second–order convergence for all the variables when the values of τ are large. However, for the smallest value of τ used in this example, sub–optimal convergence is observed in the fluid and solid velocities, while the structure displacement even exceeds the convergence rate of 2. As θ begins to increase, the rates start to deteriorate, approaching first–order convergence. We note that when $\theta = 0.5$, the errors are the smallest, which is especially apparent in the structure velocity.

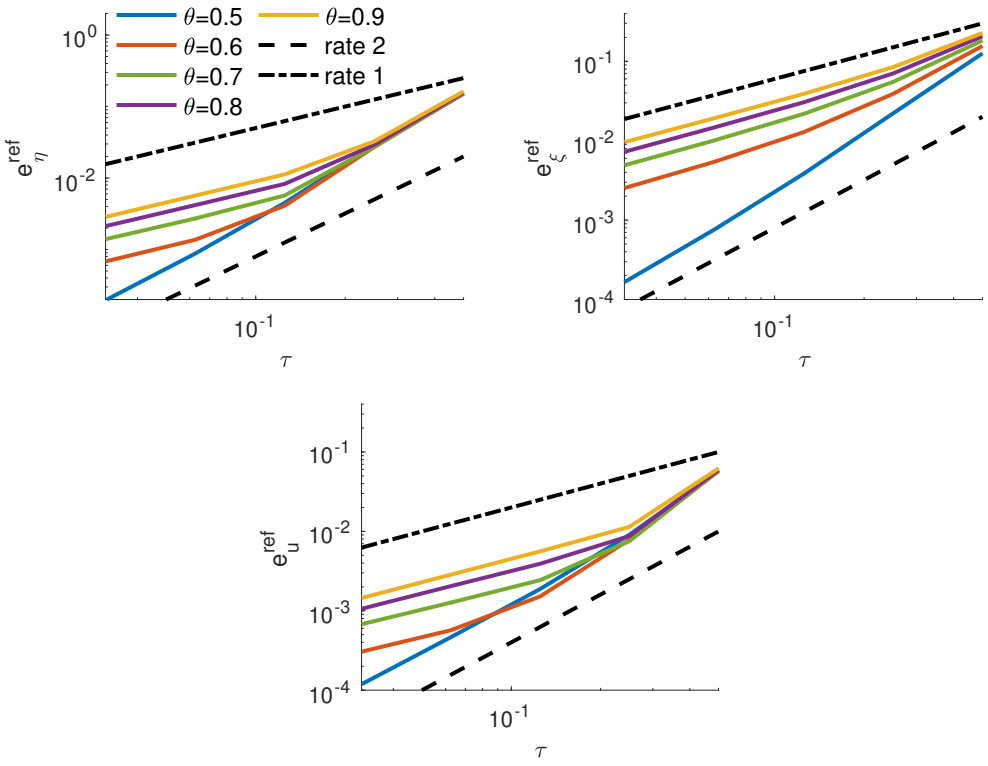

Fig. 5.2: Relative errors for the structure displacement (top–left), structure velocity (top–right), and fluid velocity (bottom) obtained using by decreasing ϵ at the same rate as τ.

To improve the sub–optimality observed in Figure 5.1, we repeat the previous simulations, but this time we decrease the tolerance ϵ at the same rate at τ. In particular, we use the following set of parameters

$$\{\tau, \Delta x, \epsilon\} = \left\{ \frac{0.02}{2^i}, \frac{0.25}{2^i}, \frac{10^{-4}}{2^i} \right\}_{i=0}^{3}.$$

Figure 5.2 shows the convergence rates across different values of θ. We note when $\theta = 0.6, 0.7, 0.8$ and 0.9, the errors for all the variables are almost identical to those in Figure 5.1. The errors also stay similar when

$\theta = 0.5$ and τ is large. However, in this case smaller errors are obtained when $\theta = 0.5$ and $\tau = 3.125 \cdot 10^{-3}$, yielding the expected second–order accuracy for all the variables.

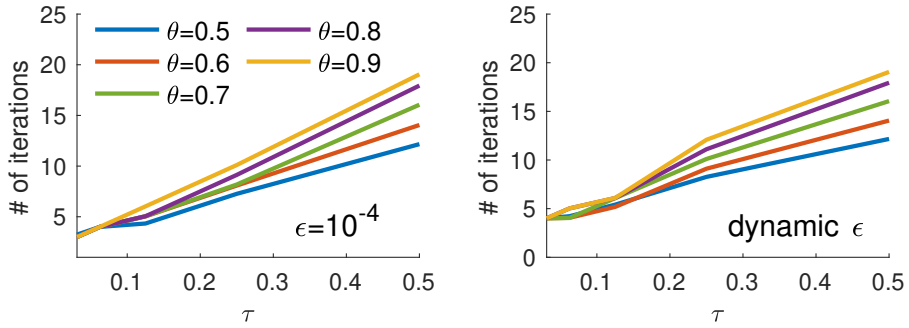

Fig. 5.3: Average number of sub–iterations obtained for different values of θ when $\epsilon = 10^{-4}$ (left) and when ϵ is changing at the same rate as τ (right).

While computing the rates of convergence, we also calculated the average number of sub–iterations needed in the iterative part of our method. Figure 5.3 shows the results obtained using $\epsilon = 10^{-4}$ (left), and the dynamic update of ϵ, where ϵ is decreased at the same rate as τ. We note that in both cases, the average number of sub–iterations decreases with τ. For the smallest value of τ, the number of sub–iterations averages around 3 when ϵ is fixed, and 4 when ϵ is changing, for all values of θ. We also note that the number of sub–iterations increases with θ, leaving $\theta = 0.5$ an excellent choice since it features the smallest number of sub–iterations, as well as the best accuracy. Across all values of θ, a slightly larger number of sub–iterations is needed when ϵ is dynamically changing.

We also compared the average number of iterations needed by Algorithm 1 and other commonly used strongly–coupled schemes in the literature. In particular, we considered the Robin–Neumann method and the Robin–Robin method described in [3,4]. The comparison of the results across different parameter values is shown in Table 5.1. We note that $\theta = 0.5$ was used in Algorithm 1. For most values considered in Table 5.1, a smaller number of sub–iterations is required by Algorithm 1 than by the Robin–Neumann and Robin–Robin methods.

τ	Δx	ρ_F	ρ_S	ϵ	RN	RR	Alg. 1
$1.25 \cdot 10^{-1}$	10^{-1}	1	1	10^{-4}	9	5	5.2
$6.25 \cdot 10^{-2}$	10^{-1}	1	1	10^{-4}	6	5	4.1
$1.25 \cdot 10^{-1}$	$5 \cdot 10^{-2}$	1	1	10^{-4}	12.9	6	4.2
$1.25 \cdot 10^{-1}$	10^{-1}	10	1	10^{-4}	9	9	5.2
$6.25 \cdot 10^{-2}$	10^{-1}	1	10	10^{-4}	4	4	3.1
$6.25 \cdot 10^{-2}$	10^{-1}	1	1	10^{-3}	7	4	4

Table 5.1: Example 1: The number of iterations required by the proposed method (Alg. 1), the Robin–Neumann (RN) method and the Robin–Robin (RR) method [4] for different parameter values.

5.2. Example 2. In this example, we consider the same setting as in Example 1, but we adapt the time step dynamically throughout the simulation instead of taking a fixed value. To adapt the time step, we compute the local truncation error for the fluid velocity, $\boldsymbol{u}$, and the structure displacement, $\boldsymbol{\eta}$, according to formula (4.2). In particular, the local truncation error is computed for u_x, u_y, η_x and η_y. The norm of the local truncation error is then computed in the L^2-sense, separately for the velocity and displacement. In particular, we compute

$$\|\hat{T}^{n+1}_{\boldsymbol{u}}\| = \left(\int_\Omega (\hat{T}^{n+1}_{u_x})^2 + (\hat{T}^{n+1}_{u_y})^2\right)^{\frac{1}{2}}, \quad \|\hat{T}^{n+1}_{\boldsymbol{\eta}}\| = \left(\int_\Gamma (\hat{T}^{n+1}_{\eta_x})^2 + (\hat{T}^{n+1}_{\eta_y})^2\right)^{\frac{1}{2}}. \tag{5.4}$$

We first compute $\|\hat{T}_{\boldsymbol{u}}^{n+1}\|$ and $\|\hat{T}_{\boldsymbol{\eta}}^{n+1}\|$ using a fixed time step, shown in Figure 5.4. We note that the error for the fluid velocity is the largest in magnitude at all times.

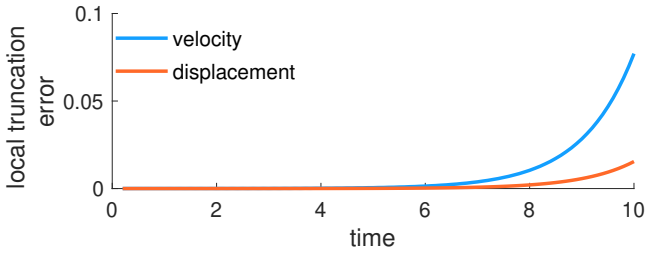

Fig. 5.4: The errors $\|\hat{T}_{\boldsymbol{u}}^{n+1}\|$ and $\|\hat{T}_{\boldsymbol{\eta}}^{n+1}\|$ computed using a fixed time step.

One way to define the local truncation error for the entire coupled problem is to take

$$\|\hat{T}^{n+1}\| = \max\{\|\hat{T}_{\boldsymbol{u}}^{n+1}\|, \|\hat{T}_{\boldsymbol{\eta}}^{n+1}\|\}.$$

We note that in this case, this is equivalent to taking $\|\hat{T}^{n+1}\| = \|\hat{T}_{\boldsymbol{u}}^{n+1}\|$. To test the performance of the method using this approach, we run the numerical simulations using the initial time step $\tau^0 = 10^{-1}$ and tolerance $\delta = 10^{-4}$. As in the previous example, $T = 10$. We take $\epsilon = 10^{-4}, \Delta x = 0.025, s = 0.95, r_{min} = 0.2, r_{max} = 1.5$ and $\theta = \frac{1}{2}$, and start the time adaptation process after 10 iterations. The parameter values are the same as in Example 1. Figure 5.5 shows the evolution of $\|\hat{T}_{\boldsymbol{u}}\|$ (top–left) and $\|\hat{T}_{\boldsymbol{\eta}}\|$ (bottom–left), as

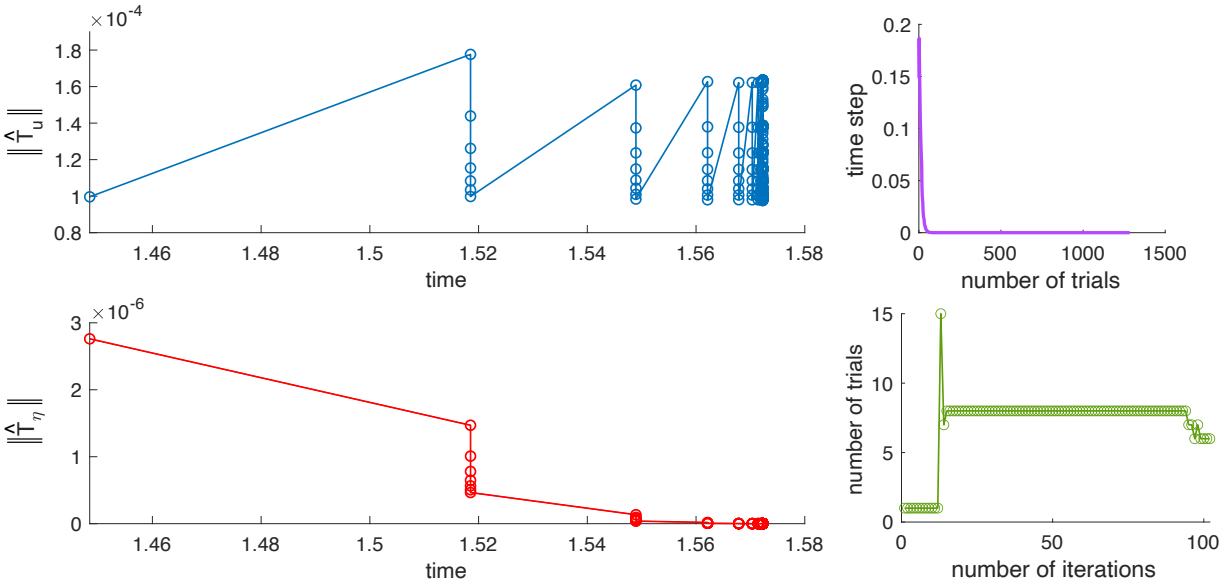

Fig. 5.5: Left: The local truncation errors for the fluid velocity (top) and the structure displacement (bottom). Right: Time evolution of the time step (top) and the number of trials in each time interval (bottom). The results were obtained defining the local truncation error as $\|\hat{T}^{n+1}\| = \|\hat{T}_{\boldsymbol{u}}^{n+1}\|$.

well as the evolution of the time step (top–right) and the number of trials needed at each iteration (bottom–right). To better illustrate the behavior of the local truncation error, $\|\hat{T}_{\boldsymbol{u}}\|$ and $\|\hat{T}_{\boldsymbol{\eta}}\|$ are shown on the interval $[1.45, 1.57]$. Due to the slow decrease of $\|\hat{T}_{\boldsymbol{u}}\|$, the time step rapidly drops, and at time $t = 1.57$ is

equal to $5.68 \cdot 10^{-33}$. In the next iteration, the time step keeps decreasing and the algorithm stops when it becomes too close to zero. Before the simulation breaks, seven trials are needed on average at each time step in order to obtain $\|\hat{T}^{n+1}\| < \delta$. We note that in contrast to $\|\hat{T}_{\boldsymbol{u}}\|$, $\|\hat{T}_{\boldsymbol{\eta}}\|$ exhibits much faster convergence to zero.

Since the $\|\hat{T}_{\boldsymbol{u}}^{n+1}\|$ dominates $\|\hat{T}_{\boldsymbol{\eta}}^{n+1}\|$, a similar dynamics is also observed when the local truncation error is defined as

$$\|\hat{T}^{n+1}\| = \left(\|\hat{T}_{\boldsymbol{u}}^{n+1}\|^2 + \|\hat{T}_{\boldsymbol{\eta}}^{n+1}\|^2\right)^{\frac{1}{2}}.$$

Therefore, to avoid the rapid decline of the time step, we define the local truncation error as

$$\|\hat{T}^{n+1}\| = \|\hat{T}_{\boldsymbol{\eta}}^{n+1}\|.$$

We perform numerical simulations using this choice of the local truncation error, and parameters $\tau^0 = 10^{-1}, s = 0.95, r_{min} = 0.2, r_{max} = 1.5$, $\delta = 2 \cdot 10^{-5}$, $\epsilon = 10^{-4}, \Delta x = 0.025$, and $\theta = \frac{1}{2}$. As in the previous example, $T = 10$, and the time adaptation starts after 10 iterations. We note that a smaller value of δ is used here compared to the previous case because $\|\hat{T}_{\boldsymbol{\eta}}^{n+1}\|$ is smaller than $\|\hat{T}_{\boldsymbol{u}}^{n+1}\|$, as shown in Figure 5.4.

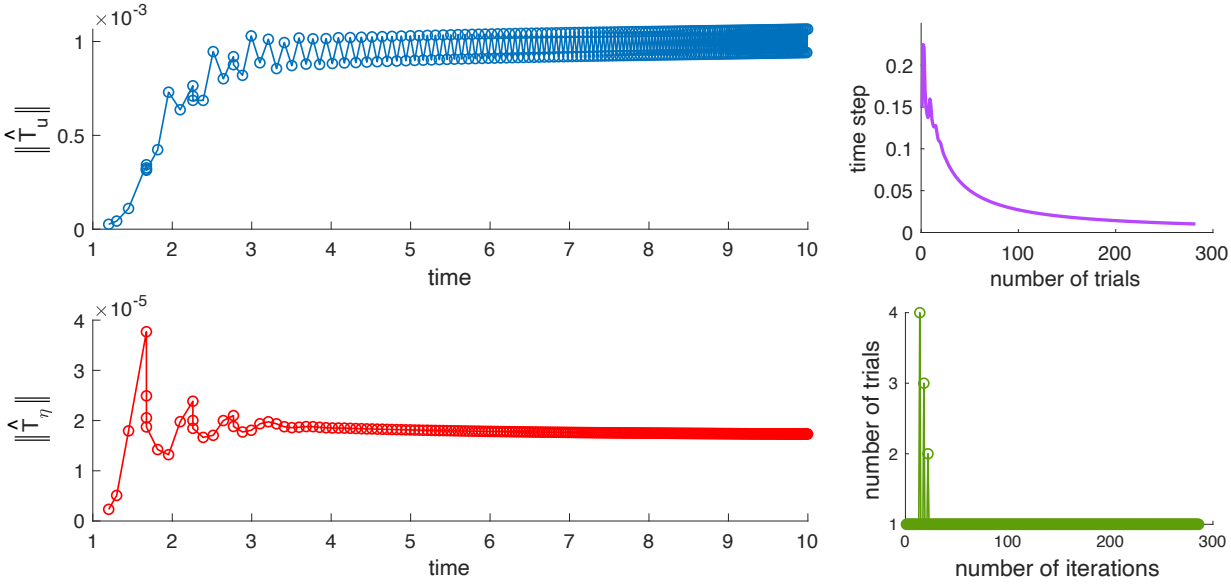

Fig. 5.6: Left: The local truncation errors for the fluid velocity (top) and the structure displacement (bottom). Right: Time evolution of the time step (top) and the number of trials in each time interval (bottom). The results were obtained defining the local truncation error as $\|\hat{T}^{n+1}\| = \|\hat{T}_{\boldsymbol{\eta}}^{n+1}\|$.

The local truncation errors $\|\hat{T}_{\boldsymbol{u}}^{n+1}\|$ and $\|\hat{T}_{\boldsymbol{\eta}}^{n+1}\|$ obtained with this choice of $\|\hat{T}_{n+1}\|$, as well as the evolution of the time–step and the number of trials are shown in Figure 5.6. Looking at the left panel, we observe that both $\|\hat{T}_{\boldsymbol{u}}^{n+1}\|$ and $\|\hat{T}_{\boldsymbol{\eta}}^{n+1}\|$ remain bounded, even though $\|\hat{T}_{\boldsymbol{u}}^{n+1}\|$ was not included in the computation of $\|\hat{T}^{n+1}\|$. The number of trials needed to satisfy $\|\hat{T}^{n+1}\| < \delta$ is greater than one only three times in the first part of the simulation, as shown in the bottom–right panel. After that, only one trial is needed for the rest of the simulation. The time step, shown in the top–right panel, is decreasing throughout the simulation, albeit slowly towards the end. The time step at the end of the simulation is equal to 10^{-2}. Since both $\|\hat{T}_{\boldsymbol{u}}^{n+1}\|$ and $\|\hat{T}_{\boldsymbol{\eta}}^{n+1}\|$ remain bounded in this example, the time step evolution is reasonable and the number of trials is low, we use $\|\hat{T}^{n+1}\| = \|\hat{T}_{\boldsymbol{\eta}}^{n+1}\|$ in the remainder of the paper.

Since it was shown in Section 5.1 that the tolerance, ϵ, used in the sub–iterative part of the algorithm needs to be varied together with the time step in order to retain a second–order convergence rate, we

also test the performance of the method using the same parameters as in the previous case, but this time adapting ϵ together with the time step. However, we set an upper bound on ϵ to preserve the accuracy of the sub–iterative solution. In particular, we set

$$\epsilon^{new} = \min\left\{\epsilon^n \min\left\{r_{max}, \max\left\{r_{min}, s\left(\frac{\delta}{\|\hat{T}^{n+1}\|}\right)^{\frac{1}{3}}\right\}\right\}, \epsilon^0\right\}, \tag{5.5}$$

and adapt it together with the time step. We perform numerical simulations by using both fixed and adaptive values of ϵ, and the adaptivity tolerances $\delta = 2 \cdot 10^{-5}$ and $2 \cdot 10^{-3}$. In each case, we count the total number of trials needed in the adaptive algorithm, and then perform simulations using Algorithm 1 with a fixed time step obtained by dividing the final time by the total number of trials. Using the same time step, we also perform simulations using the kinematically coupled $\beta-$scheme [12, 13]. For $\delta = 2 \cdot 10^{-5}$, the total number of trials is 292, and for $\delta = 2 \cdot 10^{-3}$, the total number of trials is 85. At the end of each simulation, we compute the relative error between the approximated and the exact solution. For this purpose, in addition to errors defined in (5.3), we also introduce the L^2-error for the structure displacement, defined as

$$e^{ref}_{\eta,L^2(\Gamma)} = \frac{\left\|\boldsymbol{\eta} - \boldsymbol{\eta}^{ref}\right\|^2_{L^2(\Gamma)}}{\left\|\boldsymbol{\eta}^{ref}\right\|^2_{L^2(\Gamma)}}.$$

Table 5.2 shows a comparison of the relative errors obtained using the kinematically coupled $\beta-$scheme, Algorithm 1 with a fixed time step, Algorithm 1 with a variable time step and fixed ϵ, and Algorithm 1 with a variable time step and variable ϵ. When $\delta = 2 \cdot 10^{-3}$, the errors obtained using the adaptive time–stepping are by an order of magnitude smaller than the errors obtained with methods that use a fixed time step. For a smaller value of δ, the adaptive time–stepping still gives better approximations of the fluid and solid velocities. However, errors for the displacement obtained using Algorithm 1 with fixed and variable time–stepping are comparable, but still significantly smaller than the ones obtained by the kinematically coupled $\beta-$scheme. We also note that for both values of δ, the errors obtained using the adaptive algorithm with fixed and variable ϵ are nearly identical.

$\delta = 2 \cdot 10^{-3}$	e^{ref}_u	e^{ref}_ξ	$e^{ref}_{\eta,L^2(\Gamma)}$	e^{ref}_η
kinematically coupled $\beta-$scheme	$9.51 \cdot 10^{-3}$	$8.62 \cdot 10^{-2}$	$3.14 \cdot 10^{-2}$	$3.24 \cdot 10^{-2}$
Alg. 1 w/ fixed time-step	$1.63 \cdot 10^{-3}$	$2.49 \cdot 10^{-3}$	$1.35 \cdot 10^{-3}$	$1.37 \cdot 10^{-3}$
Alg. 1 w/ adaptive time-step and fixed ϵ	$2.65 \cdot 10^{-4}$	$2.87 \cdot 10^{-4}$	$3.16 \cdot 10^{-4}$	$5.47 \cdot 10^{-4}$
Alg. 1 w/ adaptive time-step and ϵ	$2.65 \cdot 10^{-4}$	$2.86 \cdot 10^{-4}$	$3.16 \cdot 10^{-4}$	$5.47 \cdot 10^{-4}$
$\delta = 2 \cdot 10^{-5}$	e^{ref}_u	e^{ref}_ξ	$e^{ref}_{\eta,L^2(\Gamma)}$	e^{ref}_η
kinematically coupled $\beta-$scheme	$7.16 \cdot 10^{-4}$	$1.70 \cdot 10^{-2}$	$5.14 \cdot 10^{-4}$	$1.04 \cdot 10^{-3}$
Alg. 1 w/ fixed time-step	$1.47 \cdot 10^{-4}$	$2.90 \cdot 10^{-4}$	$2.44 \cdot 10^{-4}$	$5.14 \cdot 10^{-4}$
Alg. 1 w/ adaptive time-step and fixed ϵ	$3.98 \cdot 10^{-5}$	$2.52 \cdot 10^{-4}$	$2.46 \cdot 10^{-4}$	$5.29 \cdot 10^{-4}$
Alg. 1 w/ adaptive time-step and ϵ	$3.98 \cdot 10^{-5}$	$2.52 \cdot 10^{-4}$	$2.46 \cdot 10^{-4}$	$5.29 \cdot 10^{-4}$

Table 5.2: Relative errors e^{ref}_u, e^{ref}_ξ, $e^{ref}_{\eta,L^2(\Gamma)}$ and e^{ref}_η obtained using the kinematically coupled $\beta-$scheme [12, 13], Algorithm 1 with a fixed time step, Algorithm 1 with a variable time step and fixed ϵ and Algorithm 1 with a variable time step and variable ϵ.

The qualitative comparison of the results obtained using the four methods and $\delta = 2 \cdot 10^{-3}$ is shown in Figure 5.7. As expected, the results obtained using Algorithm 1 agree better with the exact solution than the results obtained using the kinematically coupled $\beta-$scheme. Looking at the zoomed–in insets, we observe that the results obtained using the adaptive time–stepping are closer to the exact solution, compared to the results obtained using the fixed time–stepping. Although the difference is very small, the second inset in the top–left panel shows that the results obtained using the adaptive method, where ϵ is adapted with the time

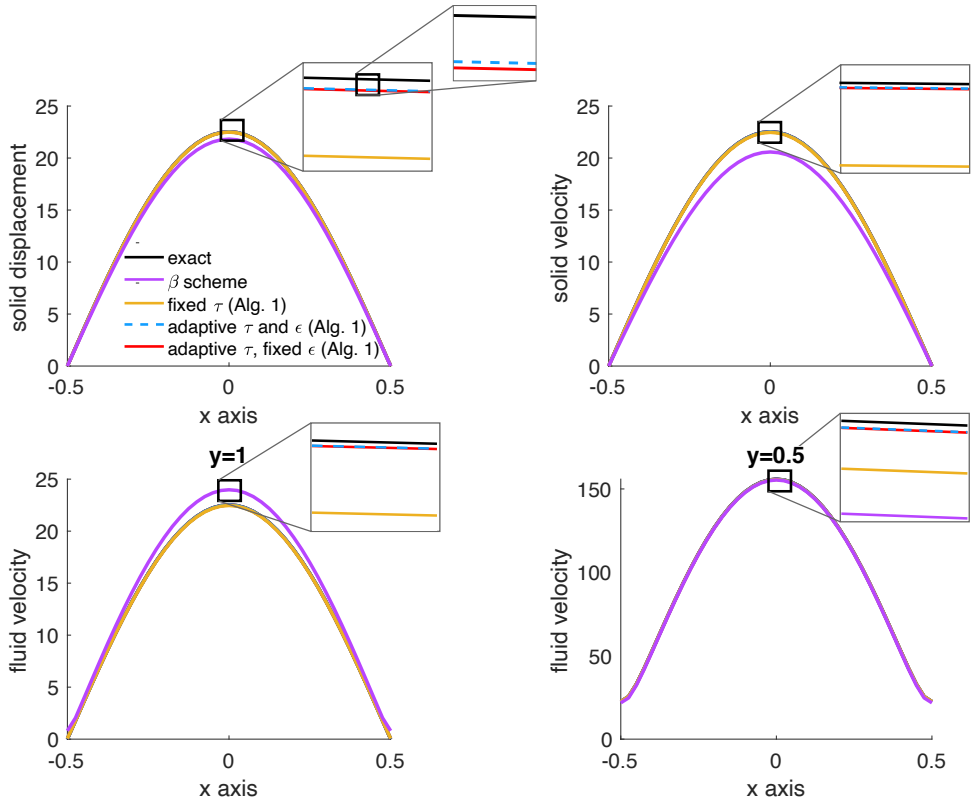

Fig. 5.7: The solid displacement (top–left), the solid velocity (top–right), the fluid velocity at the interface (bottom–left), and the fluid velocity over line $y = 0.5$ (bottom–right) obtained using $\delta = 2 \cdot 10^{-3}$.

step (blue line), are closer to the exact solution than using the same method with a fixed ϵ (red line). The same is observed for all other variables shown in Figure 5.7.

5.3. Example 3. In this example, we consider a classical benchmark problem describing the flow in a two–dimensional channel with a deformable wall. The fluid domain is $\Omega = (0, L) \times (0, R)$, where $L = 5$ cm and $R = 0.5$ cm. We assume that the top boundary is deformable, allowing only deformation in the radial direction. Hence, $\boldsymbol{\eta} = (0, \eta_y)$, and the structure dynamics is described by

$$\rho_s h \partial_{tt} \eta_y + C_0 \eta_y - C_1 \partial_{xx} \eta_y = f_{s,y},$$

where

$$C_0 = \frac{hE}{R^2(1-\nu^2)}, \qquad C_1 = \frac{hE}{2(1+\nu)},$$

and E and ν denote the Young's modulus and Poisson's ratio, respectively. We assume that the structure is fixed at the edges. At the bottom fluid boundary we prescribe symmetry boundary conditions, given by

$$u_y = 0, \quad \partial_y u_x = 0.$$

The flow is driven by prescribing a time–dependent pressure drop at the inlet and outlet sections, as defined in (2.1c)-(2.1d), where

$$p_{in}(t) = \begin{cases} \dfrac{p_{max}}{2}\left[1 - \cos\left(\dfrac{2\pi t}{t_{max}}\right)\right], & \text{if } t \le t_{max} \\ 0, & \text{if } t > t_{max} \end{cases}, \quad p_{out} = 0, \tag{5.6}$$

for all $t \in (0, T)$. The pressure pulse is in effect for $t_{max} = 0.003$ s with maximum pressure $p_{max} = 1.333 \times 10^4$ dyne/cm^2. The final time is $T = 10$ ms. The fluid and structure parameters, which are within physiologically realistic values of blood flow in compliant arteries, are given in Table 5.3. In this example, we set $\theta = \frac{1}{2}$ and initial tolerance $\epsilon^0 = 10^{-4}$, which is afterwards updated dynamically according to (5.5).

Parameters	**Values**	**Parameters**	**Values**
Fluid density ρ_f (g/cm^3)	1	**Dyn. viscosity** μ (poise)	0.035
Wall density ρ_s(g/cm^3)	1.1	**Wall thickness** h_s (cm)	0.1
Young's mod. E(dynes/cm^2)	0.75×10^6	**Poisson's ratio** ν	0.5

Table 5.3: Fluid and structure parameters used in Example 3.

We use $\mathbb{P}_2 - \mathbb{P}_1$ elements for the fluid velocity and pressure, respectively, and $\mathbb{P}_2$ elements for the structure velocity and displacement on a mesh containing 16,000 elements in the fluid domain and 400 elements in the structure domain. The problem is solved using Algorithm 1 with both fixed and adaptive time steps and the kinematically coupled $\beta-$scheme [12, 13]. The results are compared to the reference data, obtained using a second–order monolithic scheme.

We first solve the problem using Algorithm 1 with an adaptive time step. We use $\delta = 4 \cdot 10^{-4}, s = 0.95, r_{min} = 0.2, r_{max} = 1.5$, and the initial time step of $\tau^0 = 2 \cdot 10^{-4}$, resulting in 46 trials. Dividing the final time ($T = 0.0101922$) with the number of trials, we get the time step of $2.216 \cdot 10^{-4}$, which is used in the fixed time–stepping version of Algorithm 1 and the kinematically coupled $\beta-$scheme. For the monolithic method, the time step is obtained by dividing the final time by 1000. The evolution of the variable time step, compared to the value of the fixed time step obtained using this process, is shown in the top–left panel of Figure 5.8. We observe that due to the number of rejected trials, the value of the constant time step is

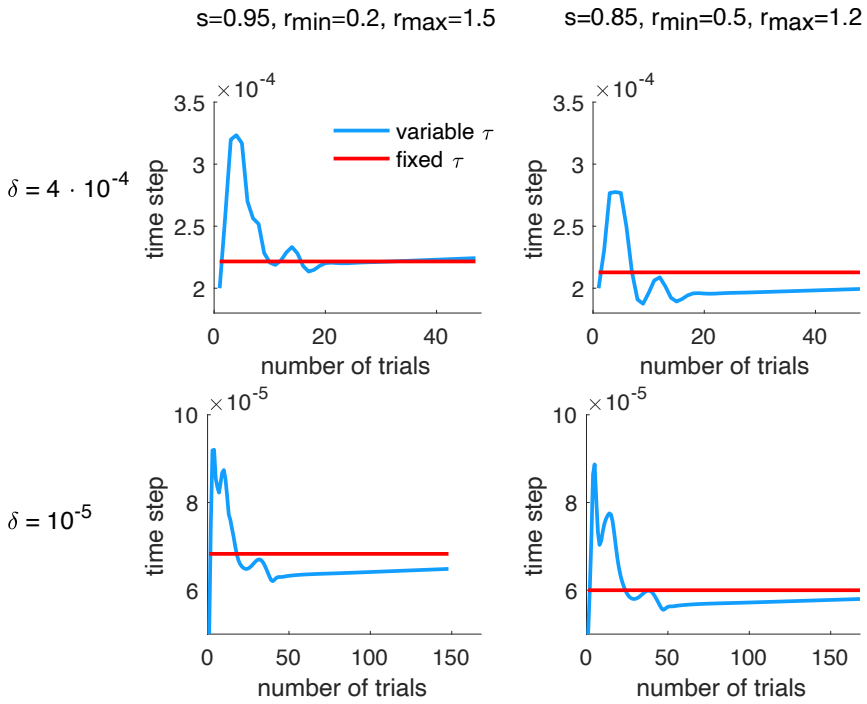

Fig. 5.8: Comparison of the variable and fixed time steps obtained using $s = 0.95, r_{min} = 0.2, r_{max} = 1.5$ (left) and $s = 0.85, r_{min} = 0.5, r_{max} = 1.2$ (right). The top row is obtained with tolerance $\delta = 4 \cdot 10^{-4}$, and the bottom row with $\delta = 10^{-5}$.

smaller than the values of the variable time step during most of the simulation. Therefore, to reduce the number of rejected trials, and to decrease the range of the possible ratios between two consecutive time steps (which is more appropriate for stiff problems such as this benchmark), we repeat the simulation using $\delta = 4 \cdot 10^{-4}, s = 0.85, r_{min} = 0.5, r_{max} = 1.2$, starting from the same initial time step of $\tau^0 = 2 \cdot 10^{-4}$. The comparison of the time step evolution of the variable time step and the fixed time step, shown in the top–right panel of Figure 5.8, indicates that in this case, the variable time step is initially larger than the fixed time step, but as the inlet pressure reduces to zero, the variable time step becomes smaller than the fixed one.

The structure displacement, and pressure and axial velocity at the bottom boundary, at the end of the simulation, are shown in Figure 5.9. The values obtained using $s = 0.95, r_{min} = 0.2, r_{max} = 1.5$ are shown in the left panel and the values obtained using $s = 0.85, r_{min} = 0.5, r_{max} = 1.2$ are shown in the right panel. As expected, since in the case shown in the left panel the fixed time step is smaller than the variable time

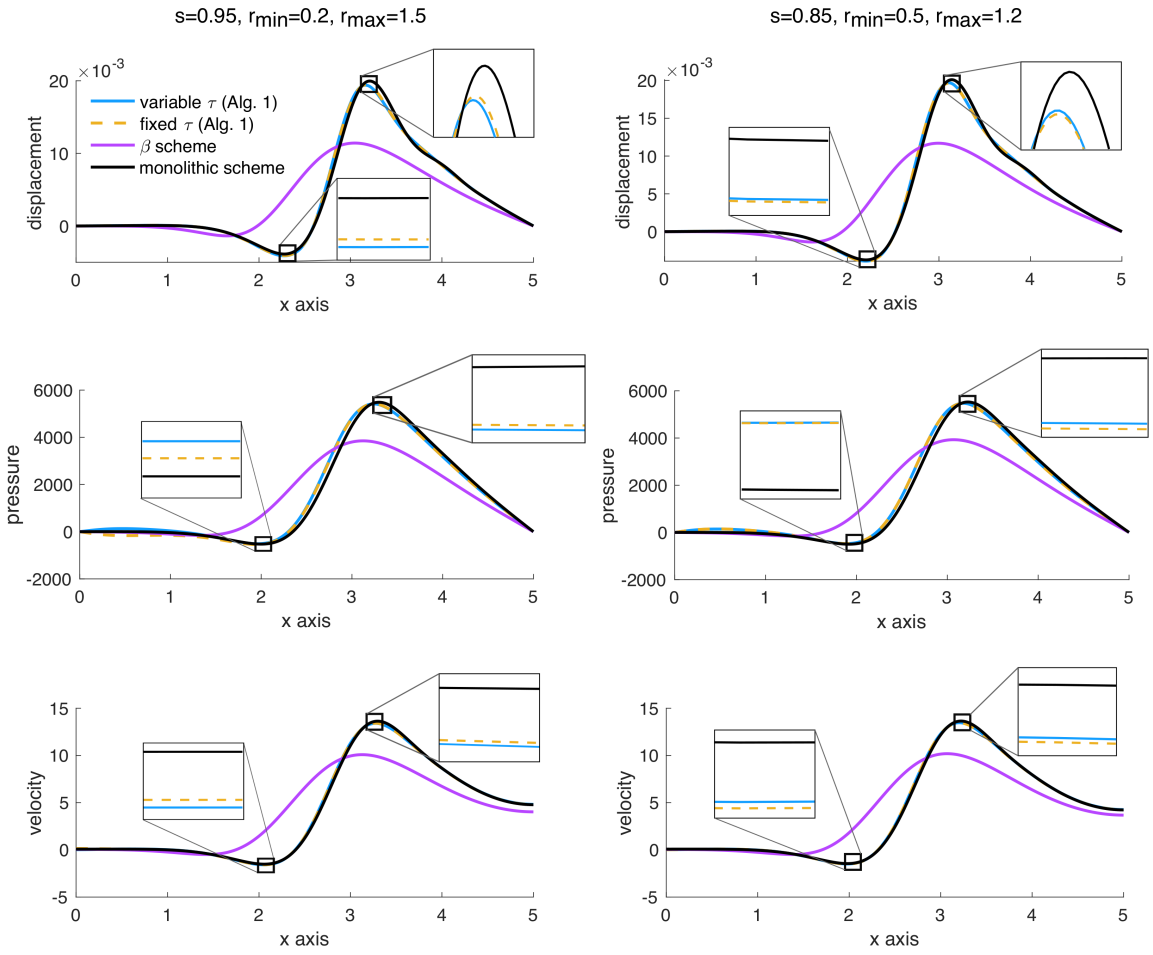

Fig. 5.9: Comparison of the structure displacement (top), pressure at the bottom boundary (middle) and axial velocity at the bottom boundary (bottom) obtained using Algorithm 1 with a variable time-step, Algorithm 1 with a fixed time-step, the kinematically coupled β scheme [12, 13], and a monolithic scheme. Algorithm 1 with a variable time-step was solved using $s = 0.95, r_{min} = 0.2, r_{max} = 1.5$ (left) and $s = 0.85, r_{min} = 0.5, r_{max} = 1.2$ (right). In both cases, tolerance $\delta = 4 \cdot 10^{-4}$ is used.

step most of the time, the results obtained using the fixed time–stepping version of Algorithm 1 are slightly closer to the monolithic results than the ones obtained using the variable time–stepping. When parameters $s = 0.85, r_{min} = 0.5, r_{max} = 1.2$ are used, the results obtained using the variable time–stepping are improved,

providing a slightly better agreement with the monolithic method than the ones obtained using the fixed time step. In both cases shown in Figure 5.8, the results obtained using the fixed and variable time–stepping versions of Algorithm 1 only slightly differ, and are very close to the monolithic ones even though relatively large time steps are used. Furthermore, they provide a significantly better agreement than the ones obtained using the kinematically coupled $\beta-$scheme.

We repeat the tests performed in this example by taking a smaller tolerance, $\delta = 10^{-5}$, and starting from a smaller initial time–step, $\tau^0 = 5 \cdot 10^{-5}$. As in the previous example, parameter sets $s = 0.95, r_{min} = 0.2, r_{max} = 1.5$ and $s = 0.85, r_{min} = 0.5, r_{max} = 1.2$ are used. The time evolution of the variable time steps is shown in the bottom panel of Figure 5.8. We observe that, as opposed to the previous example, the smaller values of the variable time step, compared to the fixed one, are obtained when $s = 0.95, r_{min} = 0.2, r_{max} = 1.5$ are used. The comparison of the structure displacement, and pressure and axial velocity at the bottom

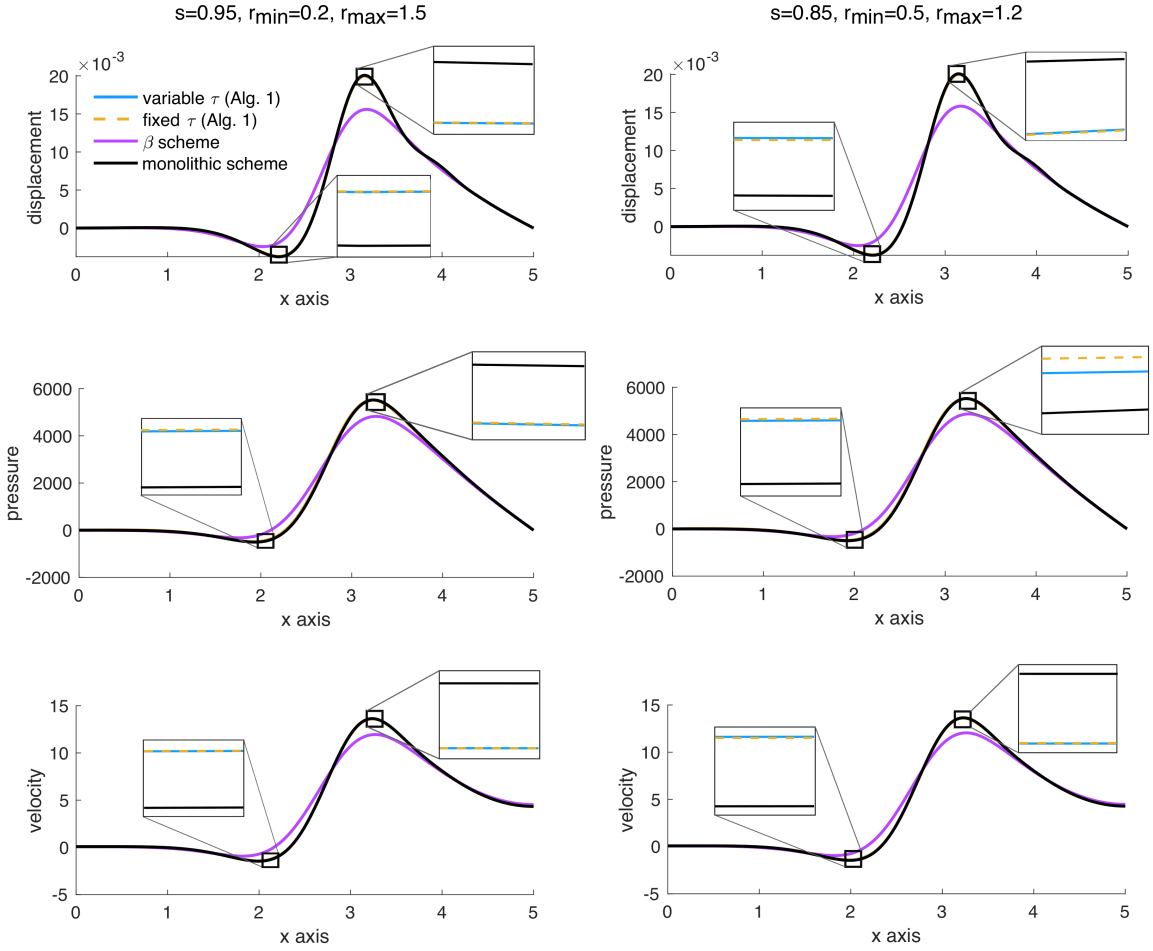

Fig. 5.10: Comparison of the structure displacement (top), pressure at the bottom boundary (middle) and axial velocity at the bottom boundary (bottom) obtained using Algorithm 1 with a variable time-step, Algorithm 1 with a fixed time-step, the kinematically coupled β scheme [12, 13], and a monolithic scheme. Algorithm 1 with a variable time-step was solved using $s = 0.95, r_{min} = 0.2, r_{max} = 1.5$ (left) and $s = 0.85, r_{min} = 0.5, r_{max} = 1.2$ (right). In both cases, tolerance $\delta = 10^{-5}$ is used.

boundary obtained using the two parameter sets are shown in Figure 5.10. We observe that the results obtained using Algorithm 1 provide an excellent agreement with the monolithic scheme. Even though there are instances where the fixed or variable versions of Algorithm 1 give slightly better approximation, overall both approaches are very close together for both sets of parameters.

6. Conclusions. We proposed a novel, adaptive, strongly–coupled partitioned method for the interaction between an incompressible, viscous fluid and a thin elastic structure. The proposed method is based on the refactorized Cauchy's one–legged '$\theta-$like' method and the kinematically coupled $\beta-$scheme. The fluid and structure sub–problems are first solved sub–iteratively until convergence, and then linearly extrapolated. This process yields a second–order convergence rate when $\theta = \frac{1}{2}$. We proved that the sub–iterative process is *linearly* convergent, and that the method is unconditionally energy bounded/stable provided $\theta \geq \frac{1}{2}$.

The algorithm is discretized in space using the finite element method, and computationally tested on three numerical examples. We note that the proposed method is novel even when it is considered with a fixed time step, in which case it can be seen as a second–order extension of the kinematically coupled $\beta-$scheme when $\beta = 1$. Therefore, in the first example, we studied the accuracy of the algorithm used with a fixed time step on a benchmark problem based on the method of manufactured solutions. We confirmed a second–order convergence rate when $\theta = \frac{1}{2}$ and the tolerance used in the sub–iterative process is changed dynamically with the time step. We also showed that even though our approach requires sub–iterations, the average number of sub–iterations needed is smaller than the one obtained by other strongly–coupled methods commonly used in the literature for most of cases considered in this study.

In the other examples, we applied the proposed algorithm using both fixed and adaptive time steps. Our results indicate that the variable time–stepping approach can have a significant advantage over a fixed time–stepping when larger adaptivity tolerances are used, yielding larger time steps, especially in less stiff benchmark problems. In stiff problems, to obtain a better performance, the parameters used in the adaptivity process need to be changed to reduce the ratio between two consecutive time steps, as well as the number of rejected trials. In both examples considered in this study, the approximations obtained using fixed and variable time–stepping versions of Algorithm 1 are nearly indistinguishable when the adaptivity tolerance is small. In both cases, an excellent agreement is observed when compared to the reference data. The extension of the method to moving domain FSI problems is out of the scope of this work and will be a subject of our future research.

7. Acknowledgements. The work of MB was partially supported by the NSF under grants DMS 1912908 and DCSD 1934300.

REFERENCES

[1] G Akrivis. Numerical methods for initial value problems. *Lecture Notes from a course taught at BCAM, Basque Center for Applied Mathematics, Bilbao, Basque Country, Spain*, 2012.
[2] U. Ascher and S. Reich. The midpoint scheme and variants for Hamiltonian systems: advantages and pitfalls. *SIAM Journal on Scientific Computing*, 21(3):1045–1065, 1999.
[3] S. Badia, F. Nobile, and C. Vergara. Fluid-structure partitioned procedures based on Robin transmission conditions. *Journal of Computational Physics*, 227:7027–7051, 2008.
[4] S. Badia, F. Nobile, and C. Vergara. Robin-Robin preconditioned Krylov methods for fluid-structure interaction problems. *Computer Methods in Applied Mechanics and Engineering*, 198(33):2768–2784, 2009.
[5] H. Baek and G. Karniadakis. A convergence study of a new partitioned fluid–structure interaction algorithm based on fictitious mass and damping. *Journal of Computational Physics*, 231(2):629–652, 2012.
[6] J. Banks, W. Henshaw, and D. Schwendeman. An analysis of a new stable partitioned algorithm for FSI problems. Part I: Incompressible flow and elastic solids. *Journal of Computational Physics*, 269:108–137, 2014.
[7] J. Banks, W. Henshaw, and D. Schwendeman. An analysis of a new stable partitioned algorithm for FSI problems. Part II: Incompressible flow and structural shells. *Journal of Computational Physics*, 268:399–416, 2014.
[8] P. Birken, T. Gleim, D. Kuhl, and A. Meister. Fast solvers for unsteady thermal fluid structure interaction. *International Journal for Numerical Methods in Fluids*, 79(1):16–29, 2015.
[9] P. Birken, K. Quint, S. Hartmann, and A. Meister. A time-adaptive fluid-structure interaction method for thermal coupling. *Computing and Visualization in Science*, 13(7):331–340, 2010.
[10] P. B. Bochev and C. Scovel. On quadratic invariants and symplectic structure. *BIT. Numerical Mathematics*, 34(3):337–345, 1994.
[11] H. Brezis. *Functional analysis, Sobolev spaces and partial differential equations*. Universitext. Springer, New York, 2011.
[12] M. Bukač, S. Čanić, R. Glowinski, J. Tambača, and A. Quaini. Fluid-structure interaction in blood flow capturing non-zero longitudinal structure displacement. *Journal of Computational Physics*, 235:515–541, 2012.
[13] M. Bukac and B. Muha. Stability and convergence analysis of the extensions of the kinematically coupled scheme for the fluid-structure interaction. *SIAM Journal on Numerical Analysis*, 54(5):3032–3061, 2016.
[14] M. Bukac, A. Seboldt, and C. Trenchea. Refactorization of Cauchy's method: a second-order partitioned method for fluid-thick structure interaction problems. *arXiv preprint arXiv:2008.12979*, 2020.

[15] M. Bukač and C. Trenchea. Boundary update via resolvent for fluid-structure interaction. *Journal of Numerical Mathematics*, 1(ahead-of-print), 2020.

[16] M. Bukač, I. Yotov, and P. Zunino. An operator splitting approach for the interaction between a fluid and a multilayered poroelastic structure. *Numerical Methods for Partial Differential Equations*, 31(4):1054–1100, 2015.

[17] J. Burkardt and C. Trenchea. Refactorization of the midpoint rule. *Applied Mathematics Letters*, 107:106438, 2020.

[18] E. Burman and M. Fernández. Stabilization of explicit coupling in fluid-structure interaction involving fluid incompressibility. *Computer Methods in Applied Mechanics and Engineering*, 198:766–784, 2009.

[19] J. Butcher and N. Goodwin. *Numerical methods for ordinary differential equations*, volume 2. Wiley Online Library, 2008.

[20] A.-L. Cauchy. *Équations différentielles ordinaires*. Éditions Études Vivantes, Ltée., Ville Saint-Laurent, QC; Johnson Reprint Corp., New York, 1981. Cours inédit. Fragment. [Unpublished course. Fragment], With a preface by Jean Dieudonné, With an introduction by Christian Gilain.

[21] M. Crouzeix and F. J. Lisbona. The convergence of variable-stepsize, variable-formula, multistep methods. *SIAM Journal on Numerical Analysis*, 21(3):512–534, 1984.

[22] G. Dahlquist. On stability and error analysis for stiff non-linear problems part i. Technical report, CM-P00069396, 1975.

[23] G. Dahlquist and A. Bjorck. *Numerical Methods*. Dover Publications, Inc., Mineola, NY. Translated from the Swedish by Ned Anderson, Reprint of the 1974 English translation, 2003.

[24] G. Dahlquist, W. Liniger, and O. Nevanlinna. Stability of two-step methods for variable integration steps. *SIAM journal on numerical analysis*, 20(5):1071–1085, 1983.

[25] P. de Sampaio, P. Hallak, A. Coutinho, and M. Pfeil. A stabilized finite element procedure for turbulent fluid–structure interaction using adaptive time–space refinement. *International Journal for Numerical Methods in Fluids*, 44(6):673–693, 2004.

[26] L. Failer and T. Wick. Adaptive time-step control for nonlinear fluid–structure interaction. *Journal of Computational Physics*, 366:448–477, 2018.

[27] M. Fernández. Incremental displacement-correction schemes for incompressible fluid-structure interaction: stability and convergence analysis. *Numerische Mathematik*, 123(1):21–65, 2013.

[28] C. W. Gear and K. W. Tu. The effect of variable mesh size on the stability of multistep methods. *SIAM Journal on Numerical Analysis*, 11:1025–1043, 1974.

[29] W. Gear. *Numerical initial value problems in ordinary differential equations*, volume 1. Prentice Hall, 1971.

[30] V. Girault and P-A. Raviart. Finite element approximation of the Navier-Stokes equations. *Lecture Notes in Mathematics*, 749, 1979.

[31] E. Godlewski and P-A. Raviart. *Numerical approximation of hyperbolic systems of conservation laws*, volume 118. Springer Science & Business Media, 2013.

[32] D. Griffiths and D. Higham. *Numerical methods for ordinary differential equations: initial value problems*. Springer Science & Business Media, 2010.

[33] E. Hairer, S. Nørsett, and G. Wanner. *Solving Ordinary Differential Equations I: Nonstiff Problems: With 105 Figures*. Springer-Verlag, 1987.

[34] E. Hairer, S. P. Nørsett, and G. Wanner. *Solving ordinary differential equations. I*, volume 8 of *Springer Series in Computational Mathematics*. Springer-Verlag, Berlin, second edition, 1993. Nonstiff problems.

[35] F. Hecht. New development in freefem++. *J. Numer. Math.*, 20(3-4):251–265, 2012.

[36] Gennady Yu. Kulikov and Sergey K. Shindin. One-leg variable-coefficient formulas for ordinary differential equations and local-global step size control. *Numer. Algorithms*, 43(1):99–121, 2006.

[37] Y. Kulikov and S. K. Shindin. On multistep interpolation-type methods with automatic control of global error. *Zhurnal Vychislitel'noi Matematiki i Matematicheskoi Fiziki. Rossiĭskaya Akademiya Nauk*, 44(8):1388–1409, 2004.

[38] J. D. Lambert. *Numerical methods for ordinary differential systems*. John Wiley & Sons, Ltd., Chichester, 1991. The initial value problem.

[39] M Lukáčová-Medvidová, G Rusnáková, and A Hundertmark-Zaušková. Kinematic splitting algorithm for fluid–structure interaction in hemodynamics. *Computer Methods in Applied Mechanics and Engineering*, 265:83–106, 2013.

[40] M. Mayr, W.A. Wall, and M.W. Gee. Adaptive time stepping for fluid-structure interaction solvers. *Finite Elements in Analysis and Design*, 141:55–69, 2018.

[41] O. Nevanlinna and W. Liniger. Contractive methods for stiff differential equations. I. *BIT. Nordisk Tidskrift for Informationsbehandling (BIT)*, 18(4):457–474, 1978.

[42] O. Nevanlinna and W Liniger. Contractive methods for stiff differential equations. II. *BIT. Nordisk Tidskrift for Informationsbehandling (BIT)*, 19(1):53–72, 1979.

[43] O. Oyekole, C. Trenchea, and M. Bukac. A second-order in time approximation of fluid-structure interaction problem. *SIAM Journal on Numerical Analysis*, 56(1):590–613, 2018.

[44] A. Seboldt and M. Bukač. A non-iterative domain decomposition method for the interaction between a fluid and a thick structure. *arXiv preprint arXiv:2007.00781*, 2020.

[45] H. Stetter. *Analysis of discretization methods for ordinary differential equations*, volume 23. Springer, 1973.

[46] Y. Yu, H. Baek, and G. Karniadakis. Generalized fictitious methods for fluid–structure interactions: analysis and simulations. *Journal of Computational Physics*, 245:317–346, 2013.